The seismic cycle at subduction thrusts: 2. Dynamic implications of geodynamic simulations validated with laboratory models

Y. van Dinther,[1,2] T. V. Gerya,[2] L. A. Dalguer,[1] F. Corbi,[3] F. Funiciello,[3] and P. M. Mai[4]

Received 23 May 2012; revised 28 November 2012; accepted 29 November 2012; published 25 April 2013.

[1] The physics governing the seismic cycle at seismically active subduction zones remains poorly understood due to restricted direct observations in time and space. To investigate subduction zone dynamics and associated interplate seismicity, we validate a continuum, visco-elasto-plastic numerical model with a new laboratory approach (Paper 1). The analogous laboratory setup includes a visco-elastic gelatin wedge underthrusted by a rigid plate with defined velocity-weakening and -strengthening regions. Our geodynamic simulation approach includes velocity-weakening friction to spontaneously generate a series of fast frictional instabilities that correspond to analog earthquakes. A match between numerical and laboratory source parameters is obtained when velocity-strengthening is applied in the aseismic regions to stabilize the rupture. Spontaneous evolution of absolute stresses leads to nucleation by coalescence of neighboring patches, mainly occurring at evolving asperities near the seismogenic zone limits. Consequently, a crack-, or occasionally even pulse-like, rupture propagates toward the opposite side of the seismogenic zone by increasing stresses ahead of its rupture front, until it arrests on a barrier. The resulting surface displacements qualitatively agree with geodetic observations and show landward and, from near the downdip limit, upward interseismic motions. These are rebound and reversed coseismically. This slip increases adjacent stresses, which are relaxed postseismically by afterslip and thereby produce persistent seaward motions. The wide range of observed physical phenomena, including back-propagation and repeated slip, and the agreement with laboratory results demonstrate that visco-elasto-plastic geodynamic models with rate-dependent friction form a new tool that can greatly contribute to our understanding of the seismic cycle at subduction zones.

Citation: van Dinther, Y., T. V. Gerya, L. A. Dalguer, F. Corbi, F. Funiciello, and P. M. Mai (2012), The seismic cycle at subduction thrusts: 2. Dynamic implications of geodynamic simulations validated with laboratory models, *J. Geophys. Res. Solid Earth*, *118*, 1502–1525, doi:10.1029/2012JB009479.

1. Introduction

[2] Our thus far limited understanding of the seismic cycle at convergent margins is a result of their complex geometry and rheology, spatial inaccessibility, and the limited observational timespan over which geophysical measurements are available. Advances in our understanding are envisioned due to amongst others numerical developments, both for large timescale subduction [e.g., *Gerya*, 2011] and small timescale dynamic rupture processes [e.g., *Madariaga and Olsen*, 2002; *de la Puente et al*., 2009; *Olsen et al*., 2009]. Combining both geodynamic and dynamic rupture approaches could help to fill the gap between large-scale and small-scale processes operating consecutively at convergent margins, thereby highlighting potential relationships between subduction dynamics and seismicity. However, before combining approaches, it is important to understand to what extent small timescale seismic processes can be analyzed with a continuum mechanics based visco-elasto-plastic numerical method typically used to simulate long-term geodynamic processes. The goal of this paper is to show that cycles of earthquakes can indeed be simulated with such a numerical method.

[3] The seismic cycle has been extensively investigated with numerical models over the last three decades, although mainly in a strike-slip setting. *Wang* [2007] concludes that the key ingredients to model the long-term, i.e., tens of thousands of years, seismic cycle at subduction thrusts, are (a) a rate-dependent friction, (b) slow tectonic loading, and (c) visco-elastic stress relaxation. However, a comprehensive

This article is a companion to *Corbi et al*. [2013] doi:10.1029/2012JB009481.

[1]Swiss Seismological Service, ETH Zürich, Zürich, Switzerland.
[2]Institute of Geophysics, ETH Zürich, Zürich, Switzerland.
[3]LET-Laboratory of Experimental Tectonics, Univ. "Roma Tre", Roma, Italy.
[4]Division of Physical Sciences and Engineering, KAUST, Thuwal, Saudi Arabia.

Corresponding author: Y. van Dinther, Swiss Seismological Service, ETH Zürich, Zürich, Switzerland. (ylona.vandinther@tomo.ig.erdw.ethz.ch)

2169-9313/13/2012JB009479

model that properly includes these ingredients in a subduction setting does not exist yet [*Wang*, 2007].

[4] Models examining surface deformation often neglect a rate-dependent friction and spontaneous stress build up (cycle ingredient a), by a-priori defining either the amount of slip or stress drop (for a subduction setting [e.g., *Savage*, 1983; *Dmowska et al*., 1988; *Cohen*, 1994; *Hirahara*, 2002] or for a review see *Wang* [2007]). Models that do evaluate stress build-up on a fault to determine whether and how much slip can occur include those with a purely rate-dependent friction coefficient (e.g., *Burridge and Knopoff* [1967]; *Carlson and Langer* [1989]; *Cochard and Madariaga* [1996]) and those with a rate-and-state dependent friction coefficient. The empirical rate-and-state dependent constitutive formulation provides a unified framework describing the characteristic dependencies of fault friction on slip rate and slip history as observed in laboratory experiments [e.g., *Dieterich*, 1979; *Ruina*, 1983]. Models that include rate-and-state friction can be split into those simulating strike-slip faults for which most of the common methodology was developed [e.g., *Tse and Rice*, 1986; *Rice*, 1993; *Ben-Zion and Rice*, 1997; *Lapusta et al*., 2000; *Zöller et al*., 2006; *Hillers et al*., 2007; *Dieterich and Richards-Dinger*, 2010] and fewer models that mainly apply the methodology to subduction thrust faults [e.g., *Stuart*, 1988; *Kato and Hirasawa*, 1997; *Liu and Rice*, 2005; *Duan and Oglesby*, 2005; *Kaneko et al*., 2010; *Hori and Miyazaki*, 2011].

[5] The second ingredient to model the seismic cycle, slow tectonic loading, is innovatively included in *Lapusta et al*. [2000]. They introduce an efficient time stepping procedure to resolve both slow quasi-static loading processes and dynamic rupture propagation within the same computational framework. These and subsequent works [e.g., *Lapusta and Rice*, 2003; *Kaneko and Lapusta*, 2008; *Noda and Lapusta*, 2010], including other mentioned rate-(and-state) dependent friction models, provided many insights in amongst others the spatio-temporal seismicity patterns and nucleation, growth, and arrest of earthquakes [*Ben-Zion*, 2008].

[6] These models often assume a simplified, homogeneous elastic bulk rheology and thereby lack a time-dependent bulk deformation component arising from viscous (and plastic) rheologies (cycle ingredient c). A viscous mantle component, which gradually relaxes applied stresses, is captured in several kinematic models and among other effects observed post- and interseismic surface displacements [e.g., *Cohen*, 1994; *Hirahara*, 2002; *Wang et al*., 2012]. *Hashimoto and Matsu'ura* [2002] confirm this finding using a model with a slip- and time-dependent fault constitutive law and a visco-elastic slip response function to calculate resulting stresses on the fault.

[7] An alternative approach that includes long-term, time-dependent deformation and brittle instabilities is presented in e.g., *Lyakhovsky et al*. [2001], *Lyakhovsky and Ben-Zion* [2008, 2009], and *Lyakhovsky et al*. [2011]. They adopt a visco-elastic thermodynamic damage rheology model with a static-kinetic friction and plastic strain to model the long-term evolution of strike-slip fault zones and earthquakes.

[8] These three ingredients, rate-dependent friction, slow tectonic stress loading, and visco-elastic stress relaxation of the medium, are included in the subduction zone model presented in this paper and in two laboratory models: in the companion paper of *Corbi et al*. [2013] (Paper 1), as well as in another layered elasto-plastic, visco-elastic laboratory model by *Rosenau et al*. [2009]. To our knowledge, numerical geodynamic models studying seismicity [e.g., *Huc et al*., 1998; *Cattin and Avouac*, 2000; *Fuller et al*., 2006; *Chery and Vernant*, 2006; *Lecomte et al*., 2012] do not include an evolving rate-dependent friction coefficient (or strain rate weakening) to simulate frictional instabilities. A rate-dependent friction has, however, been included in continuum models with stick-slip instabilities in shear bands following the Shear-Transformation-Zone (STZ) model [e.g., *Daub and Carlson*, 2008; *Daub and Carlson*, 2009]. Their model describes plastic deformation based on grain-scale physics in amorphous materials and fault gauges [*Falk and Langer*, 1998].

[9] Spontaneously developing faults are particularly important for long time scales at which faults can not be assumed stationary (i.e., tens of thousands of years and more) [*Sleep*, 2002]. Other benefits of continuum mechanic visco-elasto-plastic codes include a self-consistently evolving absolute stress distribution, a more realistic geometry with different rock assemblages, their phase transitions, and corresponding material properties, and a composite bulk rheology (including off-fault plasticity and viscous deformation). However, in the experimental setup of this study, we use a single visco-elastic wedge-shaped material, which includes the lithospheric mantle response of the overriding plate, and defines the location of a single fault zone to facilitate an understanding of this comprehensive class of models. This type of continuum visco-elasto-plastic model can be applied to analyze seismic cycle deformation in relation to long-term deformation at convergent margins and may contribute to intermediate- and long-term seismic hazard assessment.

[10] The applicability of our numerical method for seismic cycle modeling is demonstrated by validating it with results from a novel laboratory approach presented in Paper 1 [*Corbi et al*., 2013] and by exploring the range of natural features captured. The companion paper demonstrates the presence of stick slip dynamics in a visco-elastic gelatin wedge over sandpaper setting that is analog to the seismic subduction thrust system. This laboratory validation approach provides an excellent opportunity to (a) constrain the material parameters involved, (b) compare numerical and experimental results, (c) complement the strengths of both methodologies, and (d) fill the gap of an absent benchmark for seismic cycle models.

[11] This paper is the first step in a new geodynamic cycling approach and attempts to better link the geodynamic and earthquake seismology communities. Section 2 therefore provides a thorough description of our numerical modeling approach, connecting geodynamic and seismological concepts. The subsequent results section is divided in subsections that each correspond to an objective. The first section answers whether fast, short, elastic events can be modeled with a continuum mechanics based viscoelasto plastic code, and addresses the required frictional formulation (section 3.1). This section also shows that the numerical model can fit the analog earthquake cycle pattern and source parameters obtained in laboratory models described in Paper 1. Section 3.2 examines the underlying physical framework and the role of the most important material parameters: the shear modulus, friction drop, and characteristic velocity of the frictional formulation. The last results section (section 3.3) explores applications to

the natural system in terms of (a) dynamic controls on and characteristics of rupture propagation, and (b) surface displacements. Finally, the most important findings of this study are discussed in section 4, together with their implications, limitations, and a comparison to both natural observations and the laboratory findings provided in the companion paper. Additionally, the appendices include information on (a) the stability of our modeling approach, (b) source parameter selection, and (c) scaling to natural equivalents.

2. Methods

[12] This section provides a short summary of the important aspects of the numerical method adopted in the code I2ELVIS as presented in *Gerya and Yuen* [2007]. We extend this method with a slip rate-dependent friction and further provide the numerical model setup and material properties adopted in this validation. A detailed description of the laboratory methodology in terms of material properties, scaling, and model setup is provided in section 2 of the accompanying paper.

2.1. Numerical Method

2.1.1. Numerical Implementation and Conservations Equations

[13] The plane strain numerical simulations were performed using the continuum mechanics based thermo-mechanical code I2ELVIS [*Gerya and Yuen*, 2007]. The code uses an implicit, conservative finite-difference (FD) scheme on a fully staggered Eulerian grid combined with a non-diffusive Lagrangian marker-in-cell technique. The characteristics-based marker-in-cell technique is used to advect millions of randomly located particles (markers) according to a velocity field calculated on the Eulerian grid [e.g., *Brackbill and Ruppel*, 1986; *Gerya and Yuen*, 2003; *Gerya*, 2010]. This allows for the transportation and conservation of material-specific properties, even through sharply varying material property fields. Five- and eleven-point stencils of a staggered grid are used to solve for the conservation of mass (continuity equation, Equation (1)) and momentum (Equations (2) and (3)) to obtain the pressure P (defined as mean stress, positive under compression), horizontal velocity v_x, and vertical velocity v_y at each respective staggered node.

$$\frac{\partial v_x}{\partial x} + \frac{\partial v_y}{\partial y} = 0 \tag{1}$$

$$\frac{\partial \sigma'_{xx}}{\partial x} + \frac{\partial \sigma'_{xy}}{\partial y} - \frac{\partial P}{\partial x} = \rho \frac{Dv_x}{Dt} \tag{2}$$

$$\frac{\partial \sigma'_{yx}}{\partial x} + \frac{\partial \sigma'_{yy}}{\partial y} - \frac{\partial P}{\partial y} = \rho \frac{Dv_y}{Dt} - \rho g \tag{3}$$

[14] The continuity equation assumes an incompressible flow (i.e., Poisson's ratio is 0.5, and volume changes are not allowed). In the momentum equations, which include the deviatoric stress tensor components σ_{ij} and gravity acceleration g, we introduce the inertial term, represented by density ρ times the Lagrangian time derivative of the respective velocity components $\frac{Dv}{Dt}$. In this marker-in-cell formulation, density and velocity are advected with the Lagrangian markers, along with the other material properties. Note that this incompressible inertia formulation only generates shear waves and is included to regularize the solution at high slip rates (for a discussion see Appendix A.2). Finally, this implementation of inertia allows us to compare results to a quasi-static model and thereby analyze the importance of inertia in this laboratory setup. In summary, the set of equations applied is similar to the equations typically used in (earthquake) seismology. The main difference is that material compression and inertial dynamics in terms of pressure wave propagation are neglected, while gravity is included.

2.1.2. Rheological Constitutive Relations

[15] The conservation equations (Equations (1–3)) are solved by rewriting them into strain rates and velocities using a visco-elasto-plastic rheology [e.g., *Ranalli*, 1995; *Gerya*, 2010] in which the deviatoric strain rate $\dot{\epsilon}'_{ij}$ is decomposed into a viscous, elastic, and plastic component

$$\dot{\epsilon}'_{ij} = \dot{\epsilon}'_{ij(viscous)} + \dot{\epsilon}'_{ij(elastic)} + \dot{\epsilon}'_{ij(plastic)} \tag{4}$$

where

$$\dot{\epsilon}'_{ij(viscous)} = \frac{1}{2\eta} \cdot \sigma'_{ij} \tag{5}$$

$$\dot{\epsilon}'_{ij(elastic)} = \frac{1}{2G} \cdot \frac{D\sigma'_{ij}}{Dt} \tag{6}$$

$$\dot{\epsilon}'_{ij(plastic)} = \begin{cases} 0 & \text{for } \sigma'_{II} < \sigma_{yield} \\ \chi \dfrac{\partial g_{plastic}}{\partial \sigma'_{ij}} & \text{for } \sigma'_{II} = \sigma_{yield} \end{cases} \tag{7}$$

In these constitutive equations η is effective viscosity (Newtonian in this validation study), G is shear modulus, $D\sigma'_{ij}/Dt$ is the objective co-rotational time derivative of the deviatoric stress components σ'_{ij}, χ is a plastic multiplier that locally connects plastic strain rates and stresses, $g_{plastic}$ is the plastic flow potential, σ'_{II} is the second invariant of the deviatoric stress tensor ($\sqrt{\sigma'^2_{xx} + \sigma'^2_{xy}}$), and σ_{yield} is the plastic strength or maximum stress a material can sustain.

[16] The amount of elastic versus viscous deformation within the momentum equation (Equations (2) and (3)) is determined by the visco-elasticity factor Z [*Schmalholz et al.*, 2001; *Gerya*, 2010]

$$Z = \frac{G\Delta t_{comp}}{G\Delta t_{comp} + \eta_{vp}} \tag{8}$$

where Δ_{comp} is the computational timestep, η_{vp} is a viscosity-like Lagrangian parameter that accounts for both viscous and plastic deformation and is equal to η when plastic deformation is absent. The constitutive relationship between deviatoric stress and bulk deviatoric strain rate is acquired through an explicit first-order finite-difference scheme in time [e.g., *Moresi et al.*, 2003; *Gerya*, 2010], and can be written as

$$\sigma_{ij} = 2\eta_{vp}\dot{\epsilon}_{ij}Z + \sigma_{ij}{}^{0}(1 - Z) \tag{9}$$

where σ^0_{ij} is the deviatoric stress of the previous time step, corrected for advection and rotation. In this approach, a purely elastic stress formulation can be recovered in the limit when $\Delta t_{comp}G$ is much smaller than η_{vp} ($Z \approx 0$, $\sigma_{ij} \approx 2G\Delta t\dot{\epsilon}'_{ij} + \sigma_{ij}{}^{0}$), while for $\Delta t_{comp}G$ being much larger than η_{vp} we regain a purely viscous stress expression ($Z \approx 1$, $\sigma_{ij} \approx 2\eta_{vp}\dot{\epsilon}'_{ij}$).

[17] The last constitutive relation, providing the plastic component of the deviatoric strain rate, is formulated according to

the Drucker-Prager yielding model [*Drucker and Prager*, 1952] and by assuming non-dilatant, incompressible materials, which hence define a non-associated plastic flow law (Equation (8)). In this yielding model, the plastic flow potential [e.g., *Hill*, 1950; *Vermeer*, 1990; *Gerya*, 2010] is equated to the second invariant of the deviatoric stress tensor, and the yield stress is pressure dependent and defined as

$$\sigma_{yield} = C + \mu_{eff} \cdot P \tag{10}$$

where C is cohesion or residual strength at $P = 0$ Pa, and μ_{eff} is the effective friction coefficient, which is equal to the sine of the internal friction angle. This yield criterion is evaluated at each marker, which has its own set of material properties and specific stress- and slip history. Once the second invariant of the deviatoric stress tensor exceeds the pressure dependent yield stress, the stress components are isotropically corrected to satisfy the maximum strength:

$$\sigma'_{ij} = \sigma'_{ij} \cdot \frac{\sigma_{yield}}{\sigma'_{II}} \tag{11}$$

[18] Accordingly, the local viscosity-like parameter η_{vp} decreases to weaken the material and to localize deformation

$$\eta_{vp} = \eta \frac{\sigma'_{II}}{\eta\chi + \sigma'_{II}} \tag{12}$$

[19] This plastic flow formulation approximates the brittle faulting process at low temperatures and pressures [*Moresi et al*., 2003; *Buiter et al*., 2006; *Gerya*, 2010, and references therein]. Note that this invariant, mean stress formulation allows for a free evaluation of all possible localization planes, as an a priori fault plane does not need to be defined. Finally, it is important to realize that this frictional yielding formulation is not fully coupled to the conservation equations (Equations (1), (2), and (3)) as in dynamic earthquake rupture modeling. Stresses evolve independent of the yield stress in response to the conservation equations and the two are only coupled during plastic yielding.

2.1.3. Rate-Dependent Friction

[20] A slip velocity-dependent friction coefficient is incorporated in the code to describe brittle instabilities. Our innovative, local formulation is equivalent to the strongly rate-dependent friction formulation adopted in e.g., *Burridge and Knopoff* [1967]; *Cochard and Madariaga* [1994]; *Shaw and Rice* [2000]; *Ampuero and Ben Zion* [2008]. The strong dependence on slip rate V is thought to occur at seismic slip rates in nature based on recent high velocity rotary shear experiments (e.g., *Di Toro et al*. [2011]). We assume a steady-state friction, i.e. our state variable does not change with time, and use a local, point-wise approach to calculate an effective friction coefficient μ_{eff} for each marker as

$$\mu_{eff} = \mu_s(1-\gamma) + \mu_s \frac{\gamma}{1 + V/V_c} \tag{13}$$

where μ_s is the static friction coefficient, V_c is the characteristic velocity, a velocity at which half of the friction change has occurred, and γ represents the amount of slip velocity-induced weakening as

$$\gamma = 1 - \frac{\mu_d}{\mu_s} \tag{14}$$

where μ_d is the dynamic friction coefficient. This strongly rate-dependent formulation is equivalent to Equation (3) in *Ampuero and Ben Zion* [2008] for $\gamma = -(\alpha - \beta)/\mu_s$. These α and β coefficients quantify the direct and evolution effect, respectively, and are related to the classical rate-and-state friction coefficients a and b as described in Appendix A in *Ampuero and Ben Zion* [2008]. For a positive γ (0-1) or negative $\alpha - \beta$, the friction coefficients weaken asymptotically as $1/V$ to their dynamic value μ_d. A velocity-strengthening formulation is acquired for a negative γ or positive $\alpha - \beta$.

[21] In Equation (13), the local visco-plastic slip velocity V or velocity difference between two nodal interfaces is calculated as the visco-plastic strain rate times the grid size dx

$$V = \frac{\sigma_{yield}}{\eta_m} dx \tag{15}$$

where η_m is the local viscosity obtained at the previous time step, and a stable estimate of σ_{yield} is acquired through five local iterations solving Equations (10), (13), and (15) in terms of yield stress, slip velocity, and effective friction coefficient. This visco-plastic slip rate formulation assumes that slip is localized over one grid cell, while typically spontaneously forming brittle/plastic shear zones are localized on one to two grid cells (e.g., *Buiter et al*. [2006]). It also assumes that viscous strain components are negligible during faulting, which is justified on the short time scales of interest. Tests using a visco-elasto-plastic slip rate formulation revealed that elasticity within the fault zone has a negligible impact on the frictional instabilities, at least when modeled using small displacements and rotations.

2.2. Model Setup

[22] The laboratory setup of a pseudo-2D Plexiglas wedge, filled with visco-elastic gelatin (Figure 1a, and Figure 3 in Paper 1), was cast into a two-dimensional numerical setup (Figure 1b). The visco-elastic gelatin wedge (orange) with dimensions of 60×11 cm^2 (length over the surface $\times$ height, which is equivalent to about 380×70 km^2 in nature) represents a large part of the fore-arc lithosphere, including part of the continent in terms of crust and lithospheric mantle. The gelatin is underthrusted by a 10 degree dipping plate towards a far-distance laboratory backstop. The downgoing plate is covered with plastic (grey), which exhibits velocity-strengthening frictional behavior, except for the fixed region of 31 to 47 cm from the backstop, which is made up of sand paper (red). The sand paper, which demonstrates velocity-weakening behavior, represents the seismogenic zone located near the world-averaged location of 90 to 190 km from the trench [*Heuret et al*., 2011]. Numerically, we represent the thrust interface as a finite-width fault zone or frictional boundary layer of four cells in vertical direction. At the top, a free surface is approximated with a stick air approach in which a sufficiently low viscosity, low density layer is added to the top of the model domain [e.g., *Zaleski and Julien*, 1992; *Crameri et al*., 2011].

[23] The straight subducting plate (purple lower rigid body) is continuously pushed at a constant horizontal speed of -0.0039 cm·s^{-1} (which is equivalent to 8.67 cm·yr^{-1} in nature). The push decreases linearly over the width of the frictional boundary layer to zero at its top. This numerical plate velocity is reduced by 61% with respect to the -0.01 cm·s^{-1} applied in the laboratory model, since aseismic creep processes

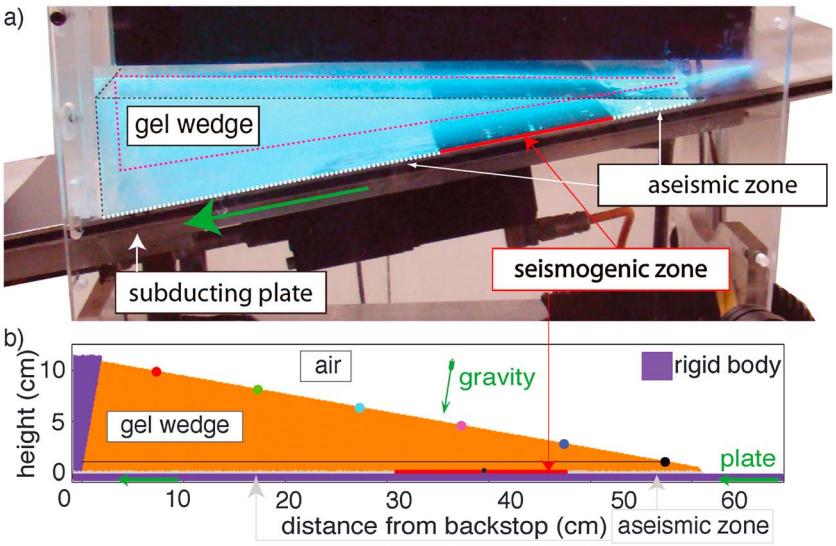

Figure 1. (a) Analog and (b) numerical model setup. The numerical setup reproduces the cross section of the analog model in the center of the analog box, and is rotated clockwise by a slab dip of 10°. Both gelatin wedges have a visco-elastic rheology, while the gelatin-sand paper and gelatin-plastic interactions are represented by a visco-elasto-plastic fault zone (shown in red and grey, denoting the seismogenic and the aseismic zone, respectively). Green arrows depict applied force (gravity) and velocity (subducting plate velocity). The black line denotes the level of all measurements done for the laboratory validation plots. Colored dots denote the location of markers that were used to acquire geodetic displacements for Figure 10. The black square shows the location of the particle properties shown in Figure 7.

in the laboratory model account for about 61% of the applied experimental push (i.e., seismic coupling is about 39%, see Paper 1, Figure 6a). Instead, interseismic locking within the numerical seismogenic zone is nearly 100%. A gravity acceleration of 9.81 m s^{-2} is applied at a slab dip angle of 10° to the gelatin surface to promote a thrust interface parallel to the rectangular grid (Figure 1b). All four boundaries have a free slip boundary condition and pressures are fixed to their neighbors at all four corners, while a pressure of 0 Pa is assigned to the leftmost top inner node.

[24] We use a regular grid size of 1 mm and each cell on average contains 16 markers. The resulting source parameter distribution converges for decreasing grid size. This convergence results from the multiplication of strain rate by grid size to obtain slip velocity (Equation (15)), which cancels the respective changes with grid size and introduces a length-scale into the plasticity problem (Appendix A3). A time step of 0.066 s is used to both solve the conservation equations and displace the markers. These time step parameters have to be chosen carefully to accurately resolve both the interseismic stress build up and the coseismic process (i.e., resolve the coseismic phase with tens of time steps). The solution is, however, to a minor extent susceptible to these time step parameters. This susceptibility is reduced by regularizing high slip rates for small time steps with incompressible inertia (Appendix A2).

2.3. Material Properties and Scaling

[25] A great advantage of this validation approach is that for most of the model parameters (Table 1) we can rely on laboratory measurements of the adopted analog materials.

[26] The visco-elastic gelatin (gel state pig skin 2.5 wt%) is thoroughly investigated in *Di Giuseppe et al.* [2009] and has a Maxwell time, the characteristic time needed to relax the applied elastic stresses, that is about three times larger than the average recurrence interval. This means that, in the current best fitting numerical model, elastic stresses are hardly relaxed during one analog earthquake cycle.

Table 1. Reference Material Properties for Each Numerical Entity, Adopted Following Guidelines Provided by Laboratory Measurements

Parameter	Symbol	Unit	Gelatin	Sand paper	Plastic	Rigid Body	Air
Min. viscosity	η_{min}	Pa·s	$3{\cdot}10^{5*}$	0.01^{*}	0.01^{*}	$1{\cdot}10^{6*}$	0.002^{*}
Max. viscosity	η_{max}	Pa·s	$3{\cdot}10^{5*}$	$3{\cdot}10^{5*}$	$3{\cdot}10^{5*}$	$1{\cdot}10^{6*}$	0.002^{*}
Shear modulus**	G	Pa	5000^{*}	5000^{*}	5000^{*}	$1.6{\cdot}10^{12*}$	5000^{*}
Density**	ρ	kg· m^{-3}	1000	1000	1000	1000	1
Static friction	μ_s	-	-	0.200	0.002	-	-
Dynamic friction	μ_d	-	-	0.035	0.157	-	-
Characteristic velocity	V_c	cm· s^{-1}	-	0.0200	0.0039	-	-
Cohesion	C	Pa	-	6	6	-	-

*For input corrected by displacement reduction factor of 100 (see main text).
**Wave speeds are 500 and 2.24 m· s^{-1} for P- and S-wave resp.

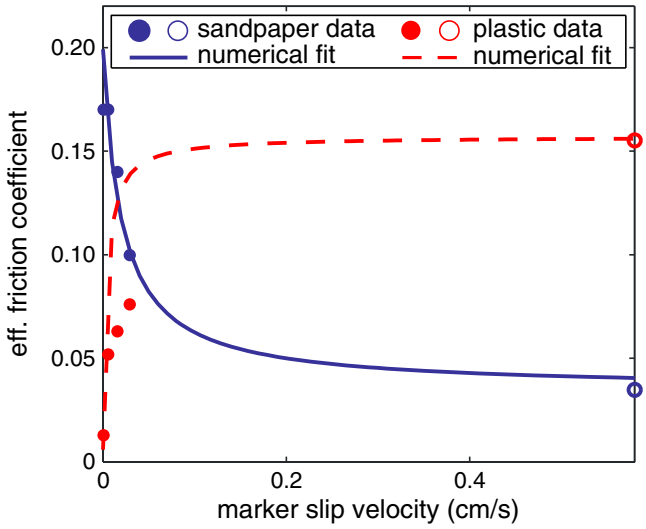

Figure 2. Friction coefficient versus slip velocity for gelatin in contact with sand paper (blue), exhibiting velocity-weakening behavior, and plastic (red dashed), exhibiting velocity-strengthening behavior. Dots represent laboratory measurements from a spring-block experiment [*Corbi et al.*, 2011], where the open dots are extrapolated assuming a logarithmic regression (with correlation coefficients of $R = 0.86$ and $R = 0.98$, respectively). The blue and red-dashed lines demonstrate the numerical effective friction coefficients used for each slip velocity based on Equations (13) and (14). Frictional parameters are provided in Table 1.

[27] The thrust contact properties of gelatin on sand paper are analyzed in detail in *Corbi et al.* [2011]. The spring block experiments in their study provide excellent data supplying effective friction coefficients for different applied slip velocities (dots in Figure 2). The lines in Figure 2 show the numerical friction formulation Equation (13) applied for the velocity-weakening behavior of sand paper (blue) and the velocity-strengthening behavior of plastic (red dashed).

[28] The range of parameters provided by the laboratory measurements serve as a reference within which we select the final parameters that best match the laboratory results. Furthermore, the material parameters of the sticky air and rigid body are chosen such that they both behave as a fully viscous bodies at the chosen computational time step (i.e., $\Delta t_{comp} > 1000\ t_{Maxwell}$). We further ensure that the effective and numerical viscosity contrasts between the air and gelatin are larger than one hundred. Additionally, a displacement limiting factor is applied to the entire model to reduce the amount of displacement and advection occurring near the singularity at the otherwise rapidly moving toe of the wedge. This means that the shear modulus and viscosity of gelatin and the frictional boundary layer (marked by a star in Table 1) are actually increased by a factor of 100, while concurrently both time steps are decreased by a factor of 100 to keep stresses and velocities the same. The values for shear moduli, viscosities, and time steps provided in this paper are kept comparable to those in the laboratory model.

[29] All material and source properties can be scaled up to natural values according to the principals of geometric, kinematic, dynamic, and rheological similarity [e.g., *Hubbert*, 1937; *Ramberg*, 1981; *Weijermars and Schmeling*, 1986]. More information about scaling, including a table with scaling parameters and the resulting natural values (Table B1), is provided in Appendix B.

3. Results and Analysis

[30] The description and analysis of the results is divided into three subsections. The first section encompasses the validation with the laboratory model and selects the most appropriate frictional formulation to match the laboratory results presented in Paper 1. The second section provides the corresponding physical framework, including a parametric study of the most important material parameters of the system. In the last section, we explore how our simulations apply to the natural system of subduction zones by analyzing the evolution of physical parameters along the thrust interface and geodetic displacements along the surface.

3.1. Validation Towards Earthquake Cycle Modeling

3.1.1. Event Characterization

[31] Prior to a comparison with laboratory data, we introduce our approach and algorithms for event selection and source parameter estimation. Following the laboratory approach (see section 2 in Paper 1) events are selected and characterized by analyzing the horizontal velocity along a line one centimeter above the analog subduction thrust. Figure 3 demonstrates the maximum seaward (i.e., in direction of the trench, blue line) and maximum landward (i.e., in direction of the laboratory backstop, magenta line) velocities along this transect. The extended time spans that show no above threshold seaward (hence landward) velocities are interpreted as interseismic periods during which the gelatin wedge is coupled to the shallow part of the downgoing plate and is thereby slowly compressed

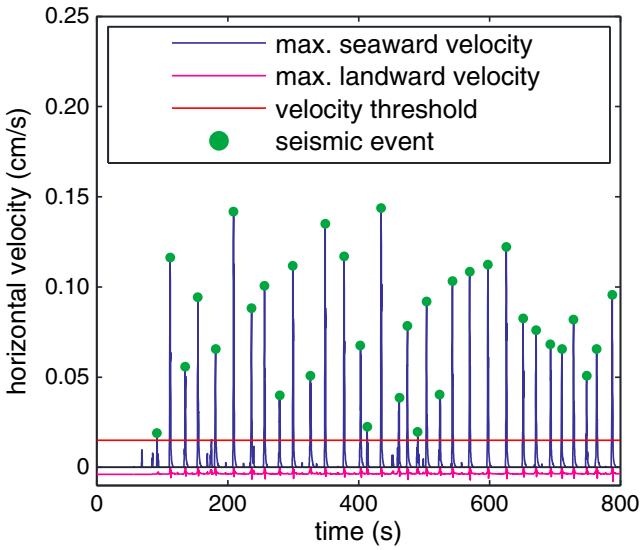

Figure 3. Peak seaward (blue line) and landward (magenta line) velocities through time. Nodal velocities are measured at a line 1 cm above the thrust interface (see Figure 1). The red line shows the velocity threshold used as a minimum seaward velocity for the selection of seismic events (green dots). The threshold is located at 3.8 times the reversed numerical push velocity (0.015 cm·s^{-1}, for a justification see Paper 1; section 2.6 and Appendix A1).

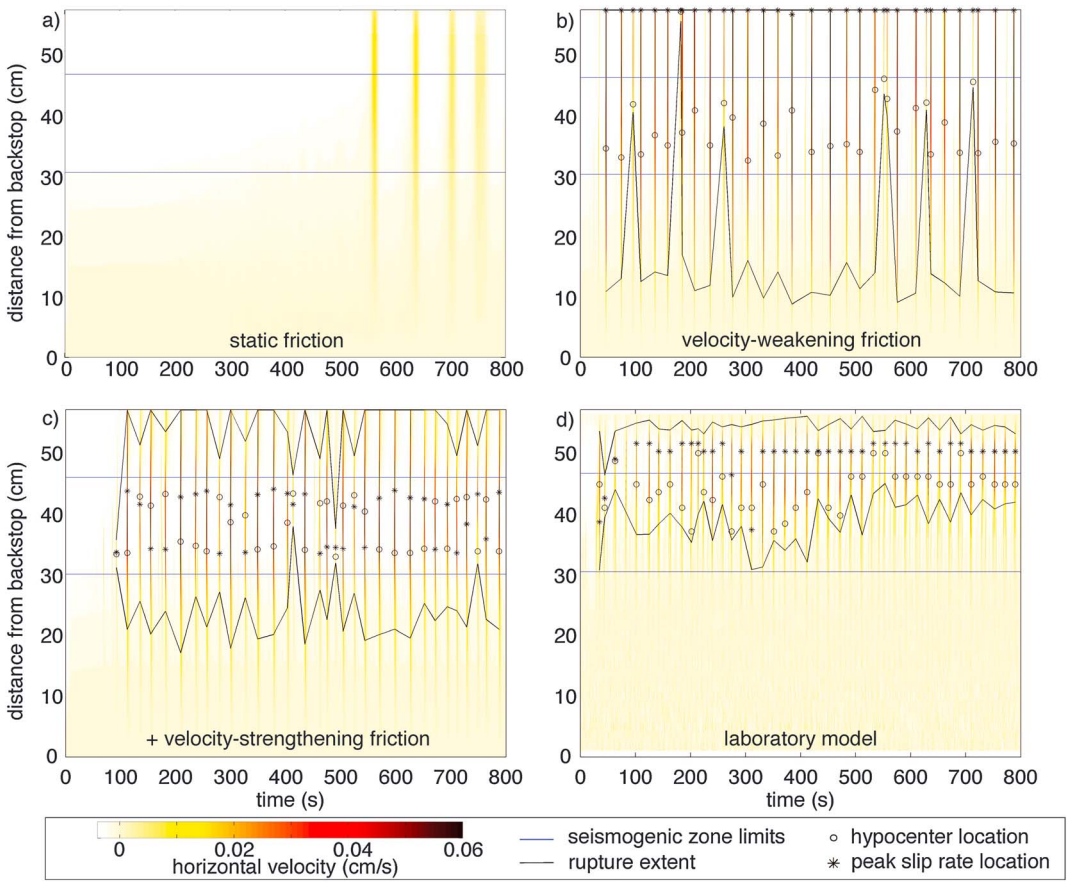

Figure 4. Spatio-temporal evolution of horizontal velocity for the reference models for different frictional formulations; (a) a static friction coefficient (parameters that deviate from the reference model: G = 800 Pa, η = 10^6 Pa·s; v_{push} = 0.0001 m·s^{-1}; and no inertia and displacement limiting factor), (b) a velocity-weakening friction coefficient within the seismogenic zone (deviating parameters: $G = 10^4$ Pa; μ_s = 0.17; μ_d = 0.06; V_c = 0.005 cm·s^{-1}), (c) reference model with a velocity-weakening friction coefficient within the seismogenic zone and a velocity-strengthening friction coefficient up- and downdip of seismogenic zone, and (d) shows the analog reference model (taken from a line in the center of the pseudo 2-D box). Several source parameters are added in black (see legend). Top represents the trench, while the bottom is at the far-field laboratory backstop. Seismogenic zone limits are added as horizontal blue lines.

against the backstop. The narrow, high seaward velocity peaks are interpreted as part of the coseismic period of an analog earthquake during which the fault ruptures and accumulated displacements are rebound toward their original location.

[32] Note that throughout this paper, the word "rupture" refers to the occurrence of rapid, threshold-exceeding slip during which permanent displacement and stress drop occur along a localized, though continuum fault zone. The accompanying short and abrupt horizontal velocity reversals are in agreement with observed horizontal geodetic displacements during subduction zone earthquakes [e.g., *Fuji and Katsumi*, 1983; *Wang*, 2007; *Simons et al*., 2011]. To identify specific events (green dots in Figure 3), we analyze the maximum seaward velocity using an algorithm that automatically identifies peaks according to three criteria: a) horizontal velocities exceed a threshold of 0.015 cm·s^{-1}, b) half widths of peaks exceed 10 data points in time, and c) events are resolved with more than three frames. The selection of the values for the first two criteria are justified in section 2.6 and Figure A1 of Paper 1.

[33] A spatiotemporal picture of horizontal velocity for each event that has passed the velocity threshold is used to obtain the source parameters for each analog earthquake (Figure A4). Appendix C explains how the extremes of the contour of the velocity threshold are used to obtain the recurrence interval and important source parameters, including a) hypocenter location, b) rupture width, c) coseismic duration, d) upward and downward rupture speeds, e) average one-sided coseismic displacement, and f) peak one-sided displacement velocity and its location.

3.1.2. Qualitative Frictional Formulation Selection

[34] To investigate the presence of periodicity, or non-constant reoccurrence of analog earthquakes, we analyze the spatiotemporal evolution of the horizontal velocity along a transect one centimeter above the thrust interface (Figure 4). Through time (x-axis) and space (y-axis), the dark yellow to red colors demonstrate different horizontal velocities towards the sea or trench (i.e., the coseismic period), while white to light yellow patches indicate regions that are moving toward the land or continent (i.e., the interseismic

period). Independent of the friction formulation, interseismic velocities decrease from the trench towards the land and are reversed during a seismic event (Figures 4a–4c). The frictional properties on the thrust interface do, however, affect the type of periodicity and the selected analog earthquake source parameters. How these observables are affected will be demonstrated in the next three subsections. In the last subsection, we select a reference frictional formulation based on a quantitative source parameter comparison with laboratory models.

3.1.2.1. Static Friction

[35] The best fitting model with a static friction coefficient, as typically used in visco-elasto-plastic continuum mechanic simulations, results in several long (minimum 20 s), slow (below threshold speeds of maximum 0.012 cm$\cdot$s^{-1}), and sometimes irregular and inconsistent seismic events (Figure 4a). These events decay with time as observed from a decrease in seaward velocity and an increase in duration. The main cause of this decay is a decrease of coupling along the interface within the interseismic period, manifested by a slight decrease in interseismic landward velocity. Additional tests show that decreasing the time step slightly decreases event duration, while also somewhat increasing the velocity, but it does not solve the problem of reduced fault coupling after several events. Within the range provided by laboratory measurements, the laboratory seismic cycle pattern can not be recovered. In summary, we observe that the presence of velocity reversals testifies that a purely pressure-dependent yield stress, i.e., a static friction, is able to generate conditions for the onset of several events. However, the lack of distinct, prolonged coupling and the absence of consistent fast and short events suggests that another mechanism for yield stress variations is required.

3.1.2.2. Velocity-Weakening Friction

[36] The mechanism generally attributed to provide this strength variation and thereby mimic frictional instabilities is velocity-weakening friction. The necessity to include this is confirmed by laboratory spring-block data that show a distinct weakening of the friction coefficient for higher slip velocities (blue dots in Figure 2). The introduction of rate-weakening friction causes a reduction in yield stress, and thereby significantly reduces coseismic duration (down to on average 1.7 s) and increases particle velocities that now reach up to 0.19 cm/s^{-1} (Figure 4b). Most importantly, however, it improves the consistency and prolongation of the periodicity, because a proper healing mechanism is acting such that when slip velocities decrease, fault strength is fully restored. For velocity-weakening friction, seaward horizontal velocities distinctly pass the velocity threshold of 0.015 cm$\cdot$s^{-1}, allowing us to identify analog earthquakes with source characteristics as explained in Appendix C (black figurations in Figure 4b). The hypocenters (open dots) are mainly located near the downdip limit of the seismogenic zone (on average $\sim$38 cm from the laboratory backstop). Occasionally, events nucleate near the updip limit of the seismogenic zone. Peak velocities (stars) are all located at the trench, as slip always accelerates towards the trench, leading to very large rupture widths (on average $\sim$39 cm). These findings demonstrate that a series of periodic fast, short analog earthquakes can be simulated if a velocity-weakening frictional formulation is employed. However, the numerical simulations still lack a mechanism that limits the acceleration and extent of the rupture into the up- and downdip aseismic regions (compare Figures 4b and 4d).

3.1.2.3. Velocity-Strengthening Friction

[37] Laboratory and natural observations [e.g., *Marone and Scholz*, 1988; *Byrne et al.*, 1988; *Hsu et al.*, 2006] show that the seismogenic zone is bounded by regions in which the sliding strength of the fault increases with slip velocity. To be consistent with these velocity-strengthening observations and the laboratory setup, rate-strengthening friction is implemented in these up- and downdip zones following laboratory spring-block data (red dots in Figure 2). The main effect of rate-strengthening friction is that rupture width is limited ($\sim$30 cm) and peak velocities are shifted to just within the seismogenic zone, on the opposite side of where the rupture nucleated. Nucleation usually occurs near the limits of the seismogenic zone, with a slight preference for the downdip limit. Consequently, a small majority of ruptures propagates upward. In summary, velocity-strengthening proves to be crucial to better reproduce several important analog and natural observations.

3.1.2.4. Quantitative Source Parameter Comparison

[38] To quantitatively compare the degree of fit with the laboratory model, we examine the average and one standard deviation of all source parameters in Figure 5. The laboratory data are taken from eight similar models to capture the variability of analog modeling results (see section 4.5 of Paper 1).

[39] We confirm that the inclusion of velocity-strengthening friction in the aseismic zones reduces the rupture width, upward rupture speed, and to a smaller extent also the amount of one-sided coseismic displacement, to at least partially within the range observed in the laboratory (blue dashed and green lines in Figure 5). However, we note that source parameters that are only related to properties within the seismogenic zone, e.g., recurrence interval and coseismic duration, could be fit equally well without velocity-strengthening.

[40] Once velocity-strengthening is included, a good agreement is obtained for the recurrence interval, one-sided coseismic displacement, coseismic duration, peak slip velocity, and both rupture speeds (compare red and green lines). The average numerical hypocenter location is, however, located 4–5 cm closer to the downdip limit of the seismogenic zone. Finally, the only source parameter whose average falls outside one standard deviation is the rupture width (Figure 4c). Considering the general variability of analog models and the unavoidable minor differences in boundary conditions, the characteristics of the most important source parameters are adequately captured. The model with a velocity-weakening seismogenic zone and a velocity-strengthening region up- and downdip is therefore selected as the reference model and will be further discussed in the remainder of the paper.

3.2. Physical Framework

[41] Following our successful validation, we analyze the physical framework and the corresponding material parameter space of our reference velocity-weakening and surrounding velocity-strengthening subduction thrust model. For an in-depth discussion of the scaling of source parameters and their values with respect to nature, including approximate estimates of earthquake size, we refer the reader to Appendix B and section 4.3 of Paper 1.

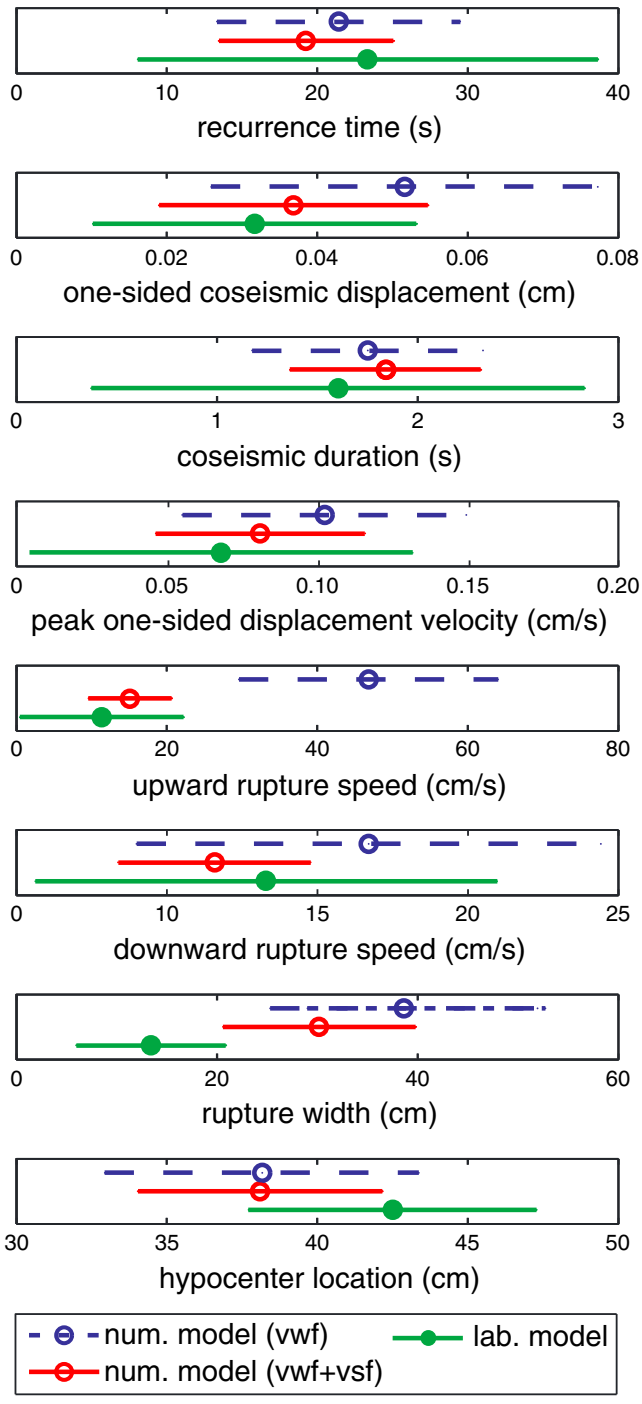

Figure 5. Degree of fit for the laboratory model (green line, filled marker) versus the numerical model both using only velocity-weakening friction within the seismogenic zone (vwf, dashed blue line, open marker) and an additional velocity-strengthening friction outside the seismogenic zone (vwf + vsf, red line, open marker). Lines represent a one standard deviation error bar around the average of the data sets. Lab models contain 215 events from eight models performed under the same experimental conditions, while the numerical experiments both contain 33 events.

3.2.1. Parameter Space Analysis

[42] The effect of several material properties on important source parameters is investigated to a) understand its variability, b) evaluate the match between numerical and laboratory models, and c) form a physical framework in which natural observations can be interpreted. Figure 6 illustrates the role of the shear modulus (panels a, d), friction drop from static to dynamic friction (panels b, e), and the velocity-weakening characteristic velocity in the frictional formulation (panels c, f) on the recurrence interval (panels a–c) and coseismic one-sided displacement (panels d–f).

[43] The shear modulus of gelatin is the most important material parameter for the interseismic period and related coseismic characteristics. It is important to note that laboratory measurements can only constrain it to be within 10^3–10^4 Pa (see grey band in Figures 6a and 6d). Within this range, an increasing shear modulus almost linearly decreases both recurrence interval and coseismic one-sided displacement (Figures 6a and 6d). Outside the laboratory defined range, even larger shear moduli result in source parameters approaching an asymptotic value, while smaller ones start to show a near exponential increase. A higher shear modulus, which corresponds to a more rigid material, also promotes slower particle velocities, shorter events, and faster rupture speeds.

[44] A larger drop from static to dynamic friction linearly increases both recurrence interval and coseismic one-sided displacement, where the impact on displacement is particularly large (Figures 6b and 6e). A larger friction drop also linearly increases particle velocities, slightly increases event duration, while rupture speeds are hardly affected.

[45] The characteristic velocity V_c incorporated in the velocity-weakening frictional formulation (Equations (13)–(15)) does not play an important role when chosen within the range suggested by laboratory measurements (Figures 6c and 6f). Larger characteristic velocities, however, show a decrease in both recurrence interval and coseismic one-sided displacements, as stress drop per event diminishes. This decrease is also observed for coseismic duration, particle velocity, and rupture width. Finally, a lower characteristic velocity, i.e., steeper drop and recovery of friction, promotes the propagation of a rupture as a pulse.

[46] The impact of other material parameters on periodicity and the observed source parameters is less significant. The viscosity of gelatin has no effect on the source parameters for viscosities larger than $5*10^4$ Pa s, which is below the minimum value suggested by laboratory measurements. The lowest non-impacting viscosity value leads to a Maxwell time of 10 s, which is almost half of the average recurrence interval (19.3 s). As the Maxwell time drops further, viscous flow starts to relax accumulated elastic stresses (as can already be seen in Figure 7d) and periodicity is increased. In summary, this means that, for the currently selected material parameters, the wedge behaves primarily in an elastic manner with minor viscous stress relaxation.

3.2.2. Physics at a Lagrangian Particle

[47] The role of velocity-weakening friction for the generation of distinct analog earthquakes is investigated by analyzing the physical properties in a Lagrangian framework of one particle located in the center of the seismogenic zone (black square in Figure 1). Figure 7 subsequently shows the markers slip velocity (panels a, b), effective

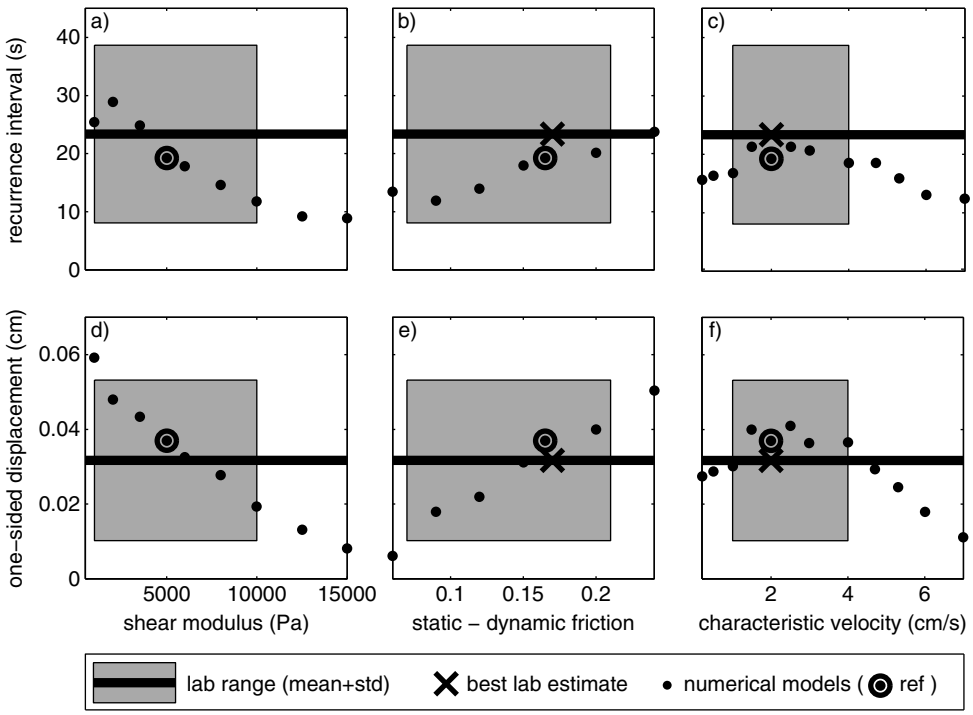

Figure 6. Effect of material and frictional properties on (a–c) the recurrence interval, and (d–f) coseismic one-sided displacement or slip. Investigated parameters are (a, d) the shear modulus of gelatin, (b, e) static minus dynamic friction coefficient (i.e., the friction drop), and (c, f) the characteristic velocity in the velocity-weakening frictional formulation (Equation (13)). Laboratory data from eight models performed under the same experimental conditions are shown as a grey band (one standard deviation, std) around the average (black, thick line). The grey band is horizontally limited to a plausible laboratory range for material parameters. The average of each numerical experiment is shown as a black dot, while the open circle denotes the described reference model.

friction coefficient (panels c, d), pressure (panels e, f), and second invariant of the deviatoric stress tensor (panels g, h).

[48] The slip velocity evolution (Figure 7a) shows a series of small and large localized events. Zooming into the analyzed reference event reveals that the slip velocity function is a slightly asymmetric, initially steeper triangle (Figure 7b).

[49] The increase in slip velocity causes the markers effective friction coefficient to drop (Figure 7c) as defined in Equation (13). The dynamic friction coefficient varies for each event as a function of its maximum slip velocity. Zooming into the typical event shows the distinct weakening and strength recovery phases as modulated by slip velocity (Figure 7d). This strength recovery, or healing of the materials strength, is crucial for subsequent stress build up and hence for to generation of new events.

[50] The yield strength of this marker is also dependent on the local pressure or mean normal stress (Figure 7e). Throughout the interseismic period, pressure increases linearly with loading time. This causes a static strength increase, even without the explicit incorporation of the evolution of the state variable. During the coseismic period we observe two main types of variations. We observe large, event-induced variations (e.g., at 693 s), which are negatively correlated to very small changes in depth ($\sim 10^{-4}$ cm) in this Lagrangian framework. Second, we observe smaller, short-term, instantaneous pressure changes during the passing of a rupture (e.g., at 524 s).

[51] Together, variations in effective friction coefficient and pressure determine the variations in yield strength of a marker (thin magenta line in Figures 7g and 7h). In our continuum formulation, the yield stress and second invariant of the deviatoric stress tensor (blue) are decoupled during the interseismic period. The second invariant increases in a slowly decreasing manner towards the yield stress. As a rupture that nucleated on a different part of the fault is approaching, stresses are instantaneously increased until the materials strength is reached. From that point onward the stress second invariant is dictated by the yield stress, or rather by the effective friction and slip velocity, until slip velocities have significantly decreased toward their interseismic value. In between the identified events, small increases in stress are observed when nearby small events occur, but for which the rupture does not reach the marker (e.g., at 589 s).

[52] Markers located at positions closer to the limits of the seismogenic zone, where most events nucleate, show stresses that may oscillate near the yield stress for some time. A similar situation in which stresses hardly increase occurs for this marker at 540 s, when nucleation occurs in the vicinity of this marker. Spontaneous nucleation occurs if neighboring markers, within a small patch of around 3–30 millimeter, reach the yield stress simultaneously. In summary, a rich evolution of local spatial and temporal features can be observed for a marker remaining roughly in the same location.

3.3. Rupture Propagation and Seismic Cycle Deformation

[53] This section describes simulated deformation features that can be compared to the natural system in the discussion

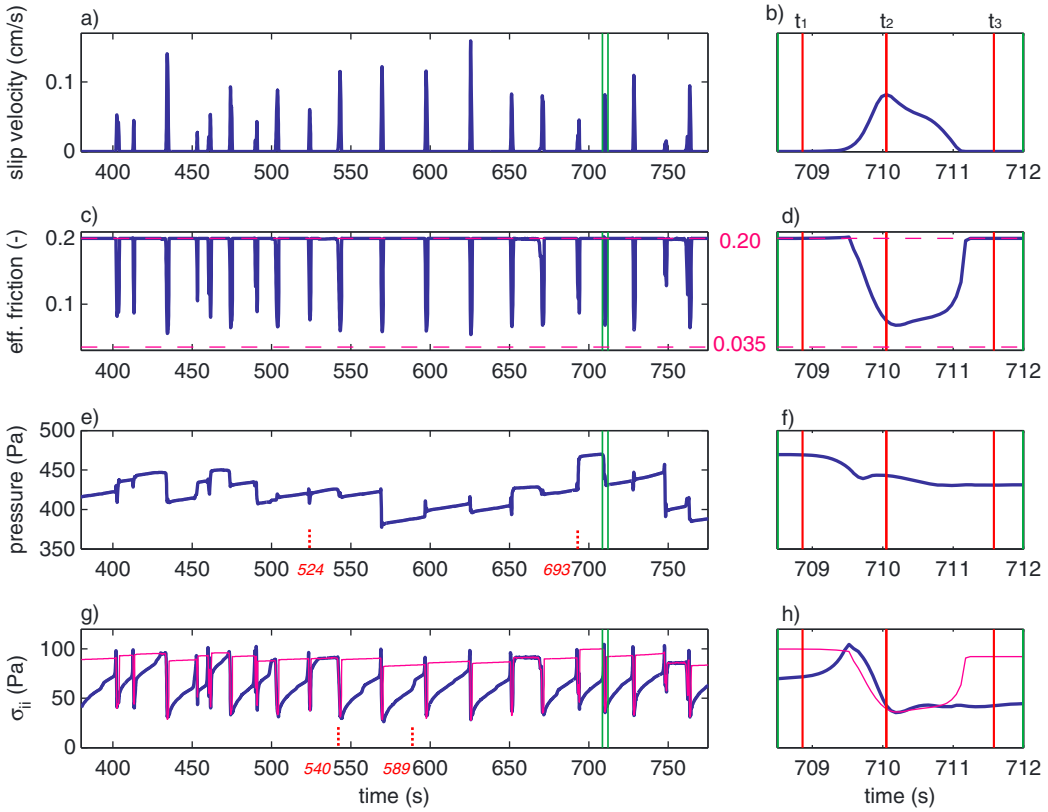

Figure 7. Lagrangian evolution of physical properties of one particle (a, c, e, g) and a zoom of a typical event delineated by green lines (b, d, f, h), which is also analyzed in Figures 8, 10, and A4. This particle is located in the center of the seismogenic zone and within the frictional boundary layer, 0.0782 cm below the contact with gelatin. Physical properties show (a, b) bulk slip velocity, (c, d) effective friction coefficient, (e, f) pressure, and (g, h) second invariant of the deviatoric stress tensor (blue line), which is compared to the yield stress (magenta line). Small, red dashed lines with corresponding time values refer to times mentioned in the text. Magenta dashed lines show static and minimum dynamic friction coefficient (c, d). Note that the zoom on stresses (panel h) shows stress slightly lacks behind the yield stress, because the yield criterion is evaluated before solving the conservation equations. Moreover, a slight misfit can be observed due to interpolation and averaging over several, possibly not all yielding, markers surrounding one node. Red vertical lines within the zoom highlight three interesting moments in time: (1) rupture initiation near the downdip limit (as defined in Figure 8b), (2) local peak slip velocity, and (3) rupture arrest (as defined in Figure 8e).

section. First, velocity, slip, and stress along the thrust interface are analyzed to relate them to indirect, seismological observables and to dynamic rupture models. Secondly, displacements at the models surface are investigated for a subsequent comparison to geodetic displacements.

3.3.1. Rupture Propagation Along Thrust Interface

[54] The propagation of the reference event (Figures 7, 10, and A4) is analyzed in terms of the spatial evolution of three characteristic rupture quantities: (a) accumulated slip, (b) nodal horizontal velocity, and (c) second invariant of the deviatoric stress tensor (Figure 8). The occurrence of active plastic slip (shown by a green bar), based on a significant viscosity drop, depicts the location of the rupture and its front, located at the limits of plastic slip within the seismogenic zone.

[55] The first snapshot shows the initial stress distribution prior to the occurrence of plastic slip within the seismogenic zone (Figure 8a). Stresses show a smooth pattern with a high and localized stress peak just before the downdip limit of the seismogenic zone, where most events nucleate.

[56] The second image shows the self-consistent heterogeneous stress conditions at the initiation of the rupture, which occurs about 4 cm downdip of the updip limit of the seismogenic zone (Figure 8b). The stress peak at the downdip limit is accompanied by several relative stress increases within the seismogenic zone, which generally correspond to the rupture limits of small previous events. Occasionally, the stress exceeds the yield stress in localized patches (e.g., at ~34 cm in Figure 8b), but rupture nucleation occurs only if that happens over a small consecutive patch of about 0.3–3 cm.

[57] The third picture depicts the downward propagation of the rupture that leads to decreased stresses behind the rupture front, while they are increased just ahead of the rupture front (Figure 8c, e.g., compare thin magenta and thick blue line). The peak velocity is located behind the rupture front near the maximum stress drop.

[58] The fourth snapshot depicts the rupture propagating in a crack-like fashion and reaching its peak slip velocity just before the downdip limit of the seismogenic zone is reached

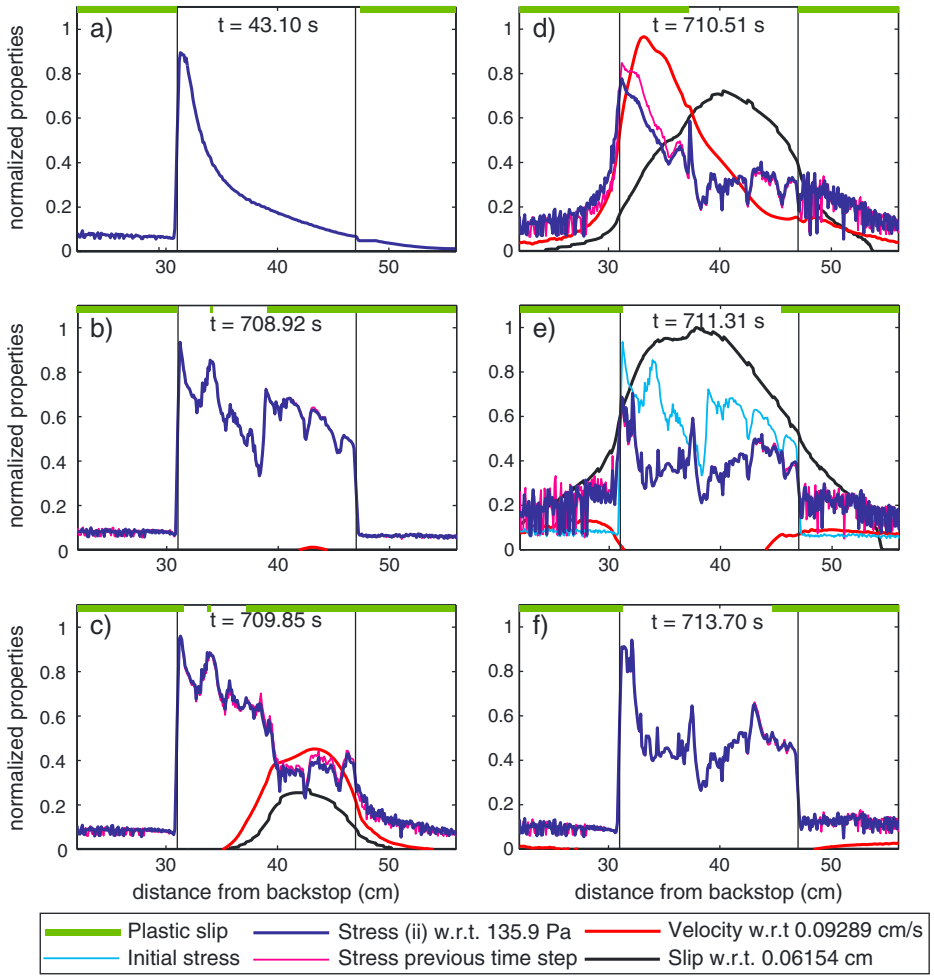

Figure 8. Evolution of a typical analog earthquake analyzed throughout this study in terms of the following normalized variables; the second invariant of the deviatoric stress tensor as acquired from the center of the fault zone (blue), nodal horizontal velocity as acquired on the hanging wall side of the fault zone (red), and accumulated slip across the fault zone (black). Slip is accumulated above the velocity threshold, here set three times smaller to capture the entire event. The top green bar indicates the location of plastic slip or yielding, defined by a large viscosity drop in the center of the fault zone. The two vertical black lines delineate the seismogenic zone. Six time snapshots highlight several interesting features: (a) initial stress distribution prior to the first plastic slip within the seismogenic zone, (b) rupture initiation near the downdip limit of the seismogenic zone, (c) rupture propagation with stress drop behind and stress increase ahead of rupture front, (d) main slip within the updip part of the seismogenic zone with healing in the downdip part, (e) rupture arrest, and (f) postseismic creep until a few seconds after the arrest.

(Figure 8d). Slip velocity near the hypocenter has decreased significantly, though slip on the gelatin side of the fault continues almost until the rupture arrests. This slip occurs, although the updip center of the fault has started to heal already, as testified by the local increased strength (i.e., viscosity in the green bar at the top) and locally increased stresses. For a minority of events, rupture occurs in a pulse-like fashion, as strength recovery occurs faster, and local points slip over a rise time as short as 20% of the total event duration.

[59] The rupture arrests at the downdip extent of the seismogenic zone in the fifth snapshot (Figure 8e). The final slip pattern shows a flattened peak in the center bounded by two relative peaks. These two relative peaks correspond to initial stress peaks, and to locations that experienced a large stress drop (see difference between thin cyan and thick blue line). The central, flattened peak in between the first two lines corresponds to a smaller stress drop (Figure 8e) and a persistent smaller decrease in viscosity (Figure 8c). Furthermore, minor slip occurs within the aseismic parts, leaving increased stresses within the vicinity of the seismogenic zone.

[60] These increased aseismic zone stresses are released to approximately their pre-event level during postseismic slip that lasts for about five seconds within the up- and downdip aseismic regions. This postseismic slip is accelerated creep with respect to the virtually continuous creep that occurs within the almost continuously yielding aseismic zones (compare velocities in panels e) and f) with respect to a) and b) in Figure 8). Postseismic slip is also observed in Figure 4c, where increased seaward velocities are present within the aseismic regions until some time after the event.

[61] A detailed analysis of thrust interface properties demonstrates several interesting features, including the existence of

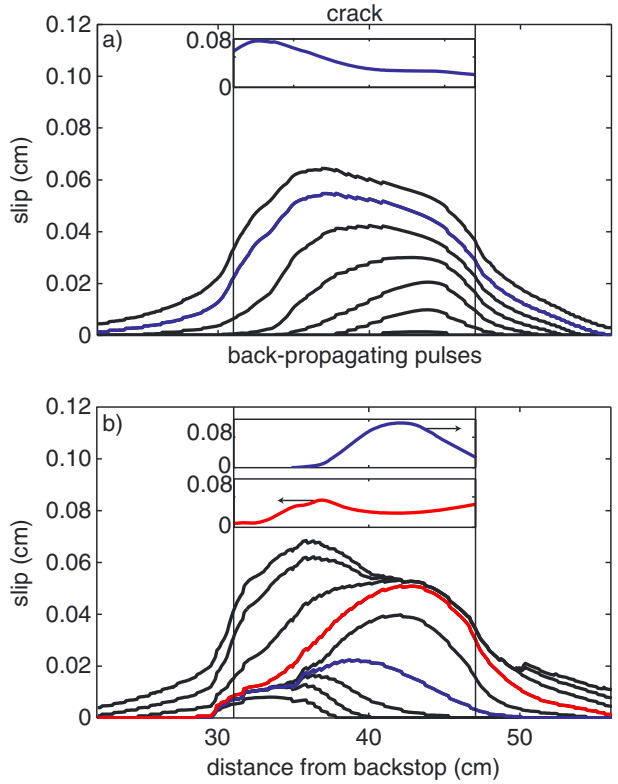

Figure 9. Rupture styles, (a) a crack at 180 s, and (b) a pulse at 402 s. Spatial distribution of slip at regular times (each 0.27 s) with insets of horizontal hanging wall-side velocity ($cm \cdot s^{-1}$) at the blue and red snapshot. The event in (b) actually shows two pulses; the first shown in the blue snapshot, and the second developing during re-rupturing of the downdip patch. Back-propagation results from reflection of the rupture front (shown in the red snapshot) on the updip seismogenic zone limit (black vertical line).

several pulses amongst a majority of cracks and re-rupturing of fault segments during the same event. The existence of cracks and pulses is also demonstrated in Figure 9 by analyzing the accumulated slip at regular time intervals. In a typical crack, once ruptured, a point keeps slipping slowly until the event arrests (Figure 9a), while slip does not accumulate in the wake of a pulse as the interface has healed (Figure 9b, both before and after the red snapshot). The red snapshot in Figure 9b separates two oppositely propagating pulses that belong to the same event. The back-propagating front of the second pulse re-ruptures the downdip patch, a phenomena observed for eight out of thirty-three cracks or pulses. Back-propagation of a rupture typically results from reflection of the opposite edge of the seismogenic zone and depends on the stress and strength evolution within the seismogenic zone. On one occasion we even observe re-rupturing starting near the hypocenter.

3.3.2. Geodetic Displacements

[62] The horizontal and vertical surface displacements are shown in Figure 10. The six lines represent observations collected from an equally spaced array of markers extending from 4 to 54 cm from the backstop (shown as colored dots in Figure 1, and equivalent to 45 to 363 km from the trench in nature). Three phases can be identified in the simulated geodetic displacements: an interseismic, coseismic, and postseismic phase.

[63] During the interseismic period all particles move toward the analog land (Figure 10a,b), and velocities decrease away from the updip limit of the seismogenic zone (dark blue line). The fastest subsidence also occurs near this updip limit (Figure 10d), while the fastest vertical uplift occurs near the downdip of the seismogenic zone (cyan line). The change from subsidence to uplift, i.e., the hinge point, occurs near the downdip limit (about 4 cm within the seismogenic zone). Displacements during the interseismic period are not linear, i.e., displacement velocities are not fully constant, as displacements generally increase toward a more sub-linear behavior.

[64] These elastic displacements rebound rapidly during the coseismic period (indicated by vertical lines in Figures 10b and 10d). This means that displacements landward of the hinge point, just within the downdip part of the seismogenic zone, subside (with largest subsidence just within the seismogenic zone), while those updip of the hinge point experience uplift.

[65] In the center of the seismogenic zone, near the average nucleation region (magenta line), one can observe a temporal pattern that includes both subsidence and uplift. The vertical component of this magenta marker shows a complex pattern that is very sensitive to small events within the seismogenic zone that are hardly observed at other surface markers. These vertical patterns depend on the corresponding slip patterns on the fault, i.e., on their amplitude, location, and number of main slip patches. The three different types of observations can be grouped depending on the complexity of the signal, i.e., the number of rapid displacement directions: a) one direction, i.e., only up or down, occurs when only a small patch of the seismogenic zone slips, b) two directions are observed when the whole seismogenic zone ruptures, and c) three directions are observed when the seismogenic zone is re-ruptured during the same event. These three groups can each be split in two, depending on the location of the hypocenter with respect to the marker. If only a small amount of slip occurs near the downdip limit of the seismogenic zone, a single upward displacement is observed (e.g., at 69 s in Figure 10), while a single downward motion is observed if slip occurs only near the updip limit. For a bi-directional temporal signal, the initial direction is equivalent to that observed for a single motion; uplift when the rupture propagates upward, subsidence when it propagates downward (e.g., at 452 s). The oppositely directed second pulse in a triple-directional signal originates when the rupture passes the station again as it re-ruptures the seismogenic zone (e.g., at 651 s).

[66] The magnitude of the overall coseismic displacement increases with the magnitude of slip and with proximity to the peak slip location of an event. Horizontal and vertical coseismic displacements decay with distance from the updip part of the seismogenic zone (that usually slips the most), with an exception of the rapidly varying vertical displacements of the magenta marker. Generally, coseismic displacements recover almost all of their interseismic displacement, except for near the trench, where noticeable permanent viscous deformation occurs. Furthermore, vertical displacements near the trench, critical for tsunami generation, depend on the updip aseismic frictional properties. For the current

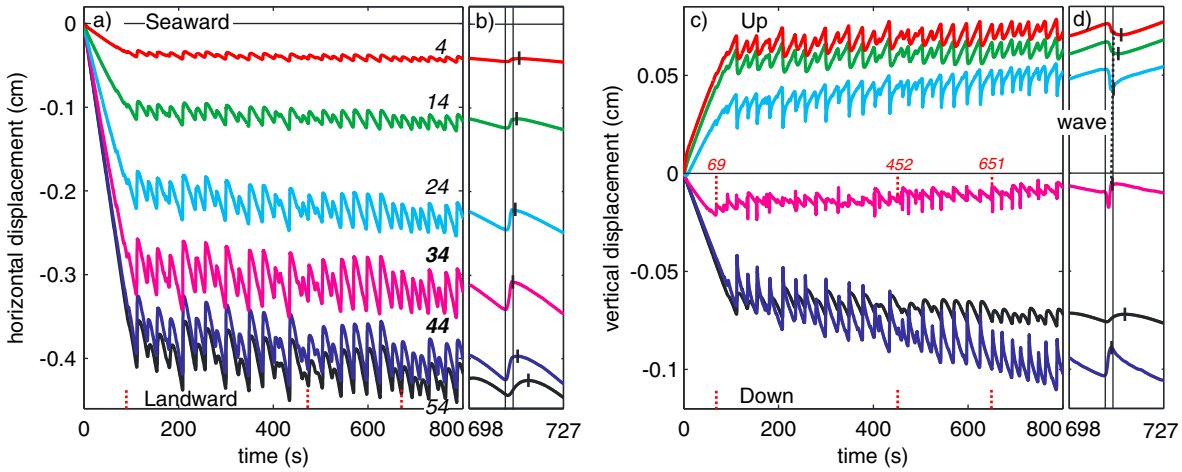

Figure 10. Particle displacements with respect to their original location as measured along the surface in (a, b) horizontal or surface-parallel, and (c, d) vertical or surface-perpendicular direction. Particles from top to bottom are located from 4 up to 54 cm from the backstop, as measured along the surface (see colored dots in Figure 1). Corresponding bold, italic locations are located above the seismogenic zone. Small red dashed lines with corresponding time values refer to times mentioned in the text. The zoom in (b) and (d) of the typical event analyzed throughout this paper includes the two surrounding interseismic periods. Vertical lines in the zoom indicate the coseismic period as defined in Figure 8. The small black lines indicate the onset of velocity reversal to its interseismic direction for each marker, while the dashed line in (d) indicates the arrival of the shear wave.

large amount of velocity-strengthening, uplift at the trench is two to three times smaller than near the updip limit of the seismogenic zone (compare black and cyan lines). For stations generally located on land, in proximity of the coast line (cyan and green lines), horizontal coseismic displacements are about two times larger than vertical displacements. Finally, these stations also show the arrival of the direct shear wave, which propagates at near the gelatin shear wave speed (dashed line in Figure 10d).

[67] Subsequent to the analog earthquake, the direction of motion is reversed back to its interseismic direction (up to short vertical lines in Figures 10b and 10d). This change occurs very rapidly and as a mainly elastic process near the epicenter. Here the region of maximum subsidence quickly becomes a region of uplift again (cyan). The markers farther inland, however, continue to move seaward throughout a longer postseismic period (red and green). The magnitude of this postseismic signal is proportional to the amount of coseismic slip.

4. Discussion

[68] The best fitting numerical model, including velocity-weakening friction within the seismogenic zone and velocity-strengthening up- and downdip of it, demonstrates the presence of a series of fast, short, elastic events, i.e., analog earthquakes, and a good match with laboratory periodicity and source parameters. The numerical model also captures a wide range of interesting natural features, such as interseismic strain accumulation, coseismic rupture propagation as cracks and re-rupturing pulses, and postseismic stress relaxation through afterslip. These features and their implications, explanations, and limitations will be discussed through a comparison to other numerical models, the companion laboratory model, and natural geodetic and seismological observations. This results in interesting implications for amongst others the role of inertia in the laboratory setup.

4.1. Role of Frictional Formulation

[69] The results show that a purely-pressure dependent yield stress, i.e., a constant friction coefficient, is able to generate several slow velocity reversals and show episodic stick-slip behavior (Figure 4a). The strain weakening that produces these events results from a decrease in pressure and hence strength as shear strain accumulates. As minor stable slip occurs in our thick fault, plastic flow that is not parallel to the displacement across the fault introduces internal elastic strains, which rotate the orientation of the principal stresses. This rotation causes a drop in pressure and could through strength lead to a slip instability [e.g., *Lecomte et al.*, 2011]. This type of strain weakening can not be observed in models with associated plasticity [e.g., *Cattin and Avouac*, 2000]. The absence of a prolonged series of localized and consistent events within the laboratory parameter range, however, demonstrates that a static friction coefficient, typically used in geodynamic simulations, is not sufficient to produce consistent earthquake cycles. This agrees with generally accepted ideas that a rate-dependent friction coefficient is necessary to generate earthquake cycles with a rapid frictional instability that subsequently heals [e.g., *Scholz*, 1998; *Ohnaka*, 2004; *Hillers et al.*, 2006; *Dieterich*, 2007; *Wang*, 2007].

[70] The models with only velocity-weakening friction within the seismogenic zone demonstrate a sequence of rather characteristic events that accelerated up to the trench and ruptured all but the deepest part of thrust (Figure 4b). These near system-wide events are the result of a successfully nucleating rupture that never meets a barrier, whose strength excess is large enough to decelerate or stop it. This diagnostic reflects the absence of a strong strength heterogeneity in combination

with a smooth stress distribution. Stress heterogeneities are small enough to be uniformly increased to the strength by the stress increase of an approaching rupture and thereby runaway to full system-wide size. By the stress increase of an approaching rupture and thereby runaway to full system-wide size. This type of behavior is characteristic for homogeneous continuum faults observed in other quasi-static, quasi-dynamic, and dynamic models [e.g., *Rice*, 1993; *Lapusta et al*., 2000; *Hillers et al*., 2006]. *Ben-Zion and Rice* [1995] explain this runaway effect based on the scaling of stress concentration ahead of the rupture front with rupture dimensions in an elastic solid. Further explanations on rupture propagation and the physics introduced by a velocity-weakening friction are provided in section 4.4.

[71] These system-wide events are suppressed if velocity-strengthening is present outside the seismogenic zone (Figure 4c). Velocity-strengthening introduces a strength increase as slip velocities go up, providing a mechanism to absorb elastic energy and thereby oppose the continuation of the rupture. This promotion of stable sliding limits the rupture widths, reduces the number of trench breaks, as observed in numerical models of e.g., *Kaneko et al*. [2008], and promotes nucleation near the updip limit of the seismogenic zone. The existence of velocity-strengthening zones up-dip of the seismogenic zone has been generally accepted as seismicity is usually sparse within a distance of about 50 km from the trench [e.g., *Byrne et al*., 1988; *Heuret et al*., 2011] and exceptionally few trench-breaking ruptures have been observed [e.g., *Byrne et al*., 1988]. The updip strengthening behavior has been attributed to several physical processes, including the stable frictional sliding of unconsolidated sediments [e.g., *Marone and Scholz*, 1988] and fault gauge lithification processes [*Saffer and Marone*, 2003].

4.2. Comparison With Laboratory Source Parameters

[72] A robust fit has been obtained for the most important source parameters of the reference model with both rate-weakening and rate-strengthening (Figure 5: red versus green lines).

[73] The only poorly reproduced feature that requires further explanation is the rupture width. The distinctly larger numerical rupture width arises, because aseismic creep is excluded in the laboratory model (i.e., the aseismic plastic does not subduct). Subduction and related interseismic stress buildup are, however, present in the numerical model. This provides more stored elastic energy, which can be released when the rupture passes.

[74] An additional comment is reserved for the hypocenter location, which is on average about 4-5 cm farther from the trench in the numerical model. This discrepancy can partially be explained by an almost twice as high snapshot rate for numerical with respect to laboratory experiments. Numerical simulations therefore capture the nucleation earlier on and nearer to its origin at the limits of the seismogenic zone.

4.3. Role of Material Parameters

[75] Stress drop and shear modulus are generally thought to be the most important parameters that determine the amount of slip. Our results show that shear modulus and friction drop (i.e., maximum stress drop) are inverse linearly correlated to the amount of slip, respectively (Figure 6). This corresponds to an accepted scaling proposed by *Abe* [1975], who observed that dislocation velocity, which is proportional to slip, is proportional to stress drop times shear velocity over shear modulus. Less rigid material behaves more elastically and can sustain larger amounts of deformation for a given stress, thereby allowing for larger slip at higher velocities, while for higher stress drops the rupture has additional energy available to slip more.

[76] The effect of material parameters on the amount of slip is always correlated to the effect on recurrence interval (Figure 6), since a longer time is needed to build up stresses again if more stress has been released during a prior event with large slip. The decrease in recurrence interval with increased rigidity can also be explained from the elastic constitutive relation (Equation (6)) in which shear modulus is proportional to elastic stress. So stresses build up faster for a larger shear modulus, and therefore reach there maximum strength earlier.

[77] The characteristic velocity within the velocity-weakening frictional formulation (Equation (13)) mainly determines the weakening rate of friction with visco-plastic slip velocity. When slip velocity is equal to the characteristic velocity, half of the weakening has occurred and the friction coefficient has a value exactly between the static and dynamic friction. Slow friction drops for large characteristic velocities lead to relatively high effective friction coefficients, and hence to a small friction drop per event. A small stress drop event slips less, and thus stresses reach the material's strength more rapidly again, leading to shorter recurrence intervals. The occurrence of more frequent events with small slip for larger characteristic velocities agrees with numerical results of *Wang* [1996] and *Ampuero and Ben Zion* [2008].

4.4. Rupture Nucleation, Propagation, and Complexity

[78] Stress build up occurs as elastic strain is accumulated within the shortening wedge. Differential loading due to a more strongly coupled seismogenic zone causes stresses to be concentrated within this zone and not along the aseismic regions (Figure 8). In these low strength regions, stresses are released continuously through aseismic creep. The main stress concentration occurs near the downdip limit of the seismogenic zone, towards which material is dragged at near plate velocities. Downdip, the weakly coupled wedge is moving much slower, so compressional stresses are locally increased and raised to close to their yield strength.

[79] The slight majority of events experiences spontaneous nucleation on this downdip, persistent increased stress patch. Nucleation at strong stress gradients, i.e., at the base of the seismogenic zone, border of an asperity, or locked patch, is in agreement with observations of large earthquakes and numerical results [e.g., *Das and Scholz*, 1983; *Dmowska et al*., 1996; *Lapusta and Rice*, 2003; *Moreno et al*., 2010]. A large-scale frictional instability results when several small, slowly slipping patches coalesce and reach a critical nucleation size [e.g., *Ruina*, 1983; *Rice*, 1993; *Lapusta et al*., 2000], which in our case is about 0.3–3 cm. The instability arises when stresses within the slowly slipping region drop enough to increase neighboring stresses to their maximum strength.

[80] When this maximum strength is reached, the instability is fed through the feedback of decreasing viscosities. This increases slip velocities, which decreases friction and strength, and which decreases viscosities even further. This

self-enhancing cycle is only impeded when stresses are released to below the yield stress. Spatial rupture propagation occurs because stresses are increased ahead of the rupture front to balance the dropping stresses in the wake of the rupture and to thereby maintain a static equilibrium (Figure 8c). This stress elevation provides the possibility to overcome patches with a large initial strength excess (Figure 7d). If these high resistance patches (either due to stress and/or strength heterogeneities) would not be there, stresses would typically be closer to the yield stress and minor slip would occur more often. This more continuous release of stresses would inhibit the occurrence of large events. The successful rupture propagation through a cascade of events as strong patches are ruptured by stress increases ahead of the rupture front is discussed by e.g., *Ohnaka* [2004] and *Ben-Zion* [2008]. Finally, ruptures arrest if the initial strength excess forms a barrier that is too high to be broken. This occurs either at increased strength or decreased stress patches within the seismogenic zone or within the aseismic velocity-strengthening regions that do not sustain large stresses.

[81] A second persistent asperity, i.e., a locked fault patch where events often nucleate, occurs near the bottom of the seismogenic zone and arises because ruptures are decelerated there and stresses are thus not fully released. Other stress heterogeneities within the seismogenic zone are mainly caused by events that arrest before the limits of the seismogenic zone are reached, since the increased stresses ahead of the rupture front are not released. These increased stress patches form asperities on which the next rupture can either nucleate or slip extensively as observed in numerical models [e.g., *Lapusta and Rice*, 2003]. Other sources of stress heterogeneities in our model include dynamic stress increases after passage of the rupture, high strength patches that resist slip and originate from variations in pressure and viscosity, and an evolving, slightly wavy slip interface topography.

[82] For further remarks on rupture characteristics and development and an extensive comparison to observations of thrust earthquakes we refer to section 4 of Paper 1. Important conclusions arising from these laboratory experiments include that their recurrence interval can be best described by a "quasi-periodic" model (section 4.1, Paper 1). Time- and slip-predictable recurrence models showed very low correlations between recurrence interval and the prior and subsequent amounts of slip, respectively ($R^2 \approx 0.19$). Our numerical models show higher correlations; $R^2 = 0.80$ for time-predictability of the purely velocity-weakening friction model, and $R^2 = 0.51$ for time-predictability of the reference model with additional velocity-strengthening. This illustrates that the predictability of numerical events is reduced for increasingly more complex systems, as suggested by, e.g., *Cochard and Madariaga* [1996], *Rosenau et al*. [2009], and *Rubinstein et al*. [2012].

[83] Furthermore, a linear proportionality between rupture width and slip with a similar proportionality constant to nature was demonstrated (Figure 9b, Paper 1). A second proportionality between seismic moment and duration demonstrated analog earthquakes follow a trend similar to regular earthquakes rather than to slow earthquakes (Figure 10 in part 1). This implies that physical principles underlying the propagation of ruptures on a gelatin-sand paper thrust interface and on a crustal wedge-oceanic slab subduction interface might be similar (section 4.4 and Figure 10, part 1).

4.5. Dynamic Implications and the Role of Inertia

[84] Results depicted in Appendix A2 demonstrate that the role of incompressible inertia, which ignores pressure waves, is minor in this laboratory setup (Figure A2, black versus grey open circle). Inertia, however, does help to regularize high slip rates, when time steps are distinctly decreased (Figure A2, black versus grey lines). We infer a minor role for inertia within the laboratory experiments with low shear strength gelatin, because the experimental results can be matched equally well with a quasi-static model without inertia. The minor contribution of inertia is explained by the low characteristic return velocity of the gelatin wedge resulting from ruptures that propagate at speeds of about 10% of the material's shear wave speed. This leads to small accelerations and hence a negligible inertial response. In the numerical model, the propagation of shear waves (with a speed of 2.24 $m \cdot s^{-1}$) is evident from the presence of one or two small surface displacement spikes during and following an event (Figure 10). Finally, we would like to emphasize that this incompressible formulation of inertia may require additional technical improvements and validation before a comparison to natural cases can be made.

[85] Our incompressible inertia, visco-elasto-plastic model, as well as the quasi-static model results not shown in this paper, capture several interesting features of dynamic ruptures. Dynamic in this sense does not only refer to wave-mediated stress transfer, but rather emphasizes the importance of temporal changes in the state of stress and deformation mechanisms observed in the system. Besides directly through the incompressible inertial term (Equations (2) and (3)), the time-dependency in these type of models is introduced through the elastic constitutive relation (Equation (6)), the loading conditions, and a rate-dependent frictional formulation. Characteristics of the dynamic behavior discussed so far include the spontaneous-rupture propagation through frictional instabilities and resulting rapid changes in stress, pressure, and slip, and its response to evolving thrust interface heterogeneities. Besides these features, we discuss two aspects that are currently intensely debated; the apparent existence of pulses and cracks, and the potential re-rupturing of a fault segment during the same event.

[86] Earthquake ruptures are thought to occur either as cracks (i.e., the ruptured fault slips continuously, Figure 9a) or as pulses (i.e., rise times are short, Figure 9b, due to rapid fault healing, Figure 8, see e.g., *Heaton* [1990]). Self-healing pulses are thought to be a consequence of the strongly rate-dependent weakening that rapidly heals the fault for low characteristic velocities [e.g., *Cochard and Madariaga*, 1994]. This is supported by our observation that pulses are barely observed for models with a high characteristic velocity and thus slower rate-dependency, as in models of *Cochard and Madariaga* [1996]. Pulses in combination with cracks have been observed in a range of numerical [e.g., *Zheng and Rice*, 1998; *Lu et al*., 2010; *Daub et al*., 2010; *Gabriel et al*., 2012] and laboratory models [e.g., *Rosakis et al*., 2007; *Corbi et al*., 2013, Paper 1].

[87] Several events showed fault segments that are re-ruptured during the same event by a rupture that propagates backward (Figure 9b). Generally, these backward propagating fronts are reflected on the imposed transition to strong velocity-strengthening friction, and are regulated by the stress and strength evolution in the wake of the rupture.

Additionally, one event was observed to re-rupture from its hypocenter onward. Re-rupturing of fault segments is currently intensely debated as it has only recently been observed with some confidence. Finite-fault earthquake source inversions with high temporal resolution show episodes of large-scale repeated slip for the 2011 M9.0 Tohoku mega-thrust earthquake [e.g., *Ide et al*., 2011]. The specific case of re-rupturing due to back-propagation is suggested for the 2010 M7.2 Sierra El Mayor strike-slip earthquake based on an eye witness account [*Hudnut*, 2011] and on regional array back-projection [*Meng et al*., 2011]. Back-propagating fronts are also recently observed in numerical [e.g., *Cochard and Madariaga*, 1996; *Noda and Lapusta*, 2010; *Gabriel et al*., 2012] and laboratory models [*Nielsen et al*., 2010].

[88] In summary, as long as a rate-dependent frictional formulation is included, several important characteristics of the seismic cycle can be captured by a continuum visco-elasto-plastic model. This conclusion is also valid for a quasi-static model, since wave-mediated stress transfer only has a minor impact in this low acceleration laboratory setup.

4.6. Geodetic Displacements

[89] Subduction zone models that have been compared to direct observations of GPS displacements generally predefine either slip or stress drop [*Wang*, 2007]. In our model, slip results spontaneously from the stress and strength evolution in response to plate convergence, gravity, and the frictional properties defined on the subduction thrust interface. Here, the three phases identified in the results – inter-, co-, and postseismic – are subsequently discussed in relation to natural observations and kinematic slip models.

[90] During the interseismic period the wedge is fully coupled to the landward-moving seismogenic zone. Downdip of the seismogenic zone, coupling is significantly reduced and velocities therefore decrease from the locked source region onward (Figure 10). The landward motion causes subsidence above the seismogenic zone, within the outer wedge, whose surface is usually located below sea level. A switch to uplift occurs at the hinge point located about 25 km seaward of the downdip limit, since just downdip of that horizontal motions are significantly decreased at the start of the decoupled aseismic zone. Uplift is largest at this maximum compression downdip transition and decays downward as the supplying source is farther away. These numerical results thus agree with numerous direct observations for the horizontal [e.g., *Dixon*, 1993] and vertical interseismic displacement components [e.g., *Aoki and Scholz*, 2003]. Furthermore, they are generally consistent with the displacement patterns predicted by the backslip model [e.g., *Savage*, 1983] and the thrust earthquake model [*Zhao and Takemoto*, 2000], if subducting plate displacements are neglected.

[91] Coseismic displacements and their magnitude are explained by the elastic rebound theory [*Reid*, 1910]. This theory can be extended to explain that those regions that accumulate most displacements interseismically, also experience most reversed coseismic slip (as confirmed by geodetic measurements of, e.g., *Moreno et al*. [2010]). This means that most coseismic subsidence occurs near the downdip limit, which is usually in the proximity of the coastline, while most coseismic uplift occurs just downdip of the updip limit. That region corresponds to the area of largest coseismic compression, since the rupture then enters the updip velocity-strengthening area and is forced to decelerate. Regional coseismic compression near the updip limit was suggested in the dynamic Coulomb wedge theory [*Wang and Hu*, 2006; *Wang and He*, 2008]. Effectively, the strong velocity-strengthening in our models restricts vertical trench displacements, important for tsunami generation, and makes them comparable to displacements near the coast line. These general horizontal and vertical patterns with subsidence at land and uplift seawards are in agreement with observations, both geologically [e.g., *Plafker*, 1972] and geodetically, as observed for e.g., for the recent M8.8 Maule and M9.0 Tohoku earthquakes [e.g., *Moreno et al*., 2010; *Ito et al*., 2011]. The location of maximum subsidence near the downdip extent of the rupture also agrees with elastic dislocation modeling results [e.g., *Wang*, 2007]. The velocity reversal and main uplift and subsidence inter- and coseismic characteristics correspond to the laboratory model presented in Paper 1, but for a few centimeter, along-thrust hinge point shift.

[92] Furthermore, our results imply that the best spatio-temporal slip inversion results may be obtained from the vertical component of stations located in the center of the seismogenic zone. Coseismic slip distributions could be recovered from the complex vertical motions at the magenta station in Figure 10c, while slip distributions and more specifically the re-rupturing of a fault segment could not be determined from signals at other stations. Possible future sea bottom instrumentation, located above the center of the observationally determined seismogenic zone, may therefore provide spatial and temporal constraints on the rupture and thereby greatly improve slip inversions. The complex vertical displacement signal is explained by the rupture direction with respect to the station; a rupture propagating toward the station leads to a small uplift, while minor subsidence is observed for a rupture propagating away from it. These motions are in agreement with a bi-lobal displacement pattern observed at the thrust (see also Figure 8g in Paper 1), representing half of the P-wave radiation pattern quadrants.

[93] Coseismic slip on a fault produces a short-term elastic rebound discussed above and a longer term visco-elastic postseismic response. The two main postseismic surface characteristics observed both in our model and in nature are the large postseismic coastal uplift rates [e.g., *Thatcher*, 1984; *Khazaradze and Klotz*, 2003] and the persisting seaward motions on land that catch up with the total coseismic slip [e.g., *Savage et al*., 1999]. The first, fast coastal uplift response can be explained by the rapid re-locking and loading of the seismogenic zone. The second, persistent seaward motion response is generally attributed to visco-elastic stress relaxation within the mantle [*Wang*, 2007]. However, in our current model, we only capture part of the response of the lithospheric mantle from the overriding plate, and stresses within the mantle beneath the slab can not be relaxed. The persistent seaward motions can also be explained by accelerated postseismic creep or afterslip on the thrust fault (Figures 4c and 8e and 8f), an alternative advocated by many authors [e.g., *Savage and Burford*, 1970; *Barrientos et al*., 1992; *Perfettini and Avouac*, 2004]. Deep and

shallow accelerated afterslip result from increased stresses, adjacent to the velocity-weakening fault segment, which are relaxed in a velocity-strengthening environment [e.g., *Tse and Rice*, 1986; *Perfettini et al*., 2005]. If velocity-strengthening is absent, adjacent stresses are already relaxed during the rupture, and consequently afterslip is negligible (Figure 4b). This mechanism is supported by the model and natural observation that transient postseismic motions are proportional to coseismic slip [e.g., *Thatcher*, 1983]. Larger coseismic slip causes higher stresses in the adjacent velocity-strengthening areas that need to be relaxed over a longer time. This argument in favor of afterslip is just a small contribution to the long-standing debate about the relative contributions of deep fault afterslip versus visco-elastic mantle stress relaxation [e.g., *Wang*, 2007]. Finally, we would like to note that viscous stress relaxation within the fore-arc does play a part in the interseismic response as evident from the non-stationary reloading of interseismic stresses (Figure 7d).

[94] Summarizing, the most important features of geodetic displacements were captured using this simple but self-consistent visco-elastic wedge model with a plastic fault formulation including rate-dependent friction. Finally, we note that the displacements, when scaled to natural values, are an order of magnitude too large (10's-100's of m), because the coseismic slip is an order of magnitude too large (as explained in Appendix B). Subsequently, this too large slip is transferred to the surface and not absorbed within the medium due to the incompressible character of gelatin and the absence of off-fault plasticity. This, however, does not affect the above qualitative and relative observations and is comparable to the tenth of a millimeter coseismic topography change observed in the laboratory model (Figure 8f in Paper 1).

4.7. Model Limitations

[95] In nature, earthquake ruptures occur within a three-dimensional, geometrically complex fault system with various scales of downdip and along-strike variations in its seismogenic behavior [e.g., *Bilek and Lay*, 2002]. The lateral, third dimension is absent in our numerical model, and restricted in the laboratory experiments. Further complexities, such as off-fault plasticity, plate bending, and most of the visco-elastic mantle relaxation, are also neglected in this simplified laboratory setup. These features are, however, included in more realistic subduction setups typically used for this modeling approach [e.g., *Gorczyk et al*., 2007]. Furthermore, our continuum-mechanics based approach does not simulate infinitely thin faults that can break in a brittle manner. It rather simulates a subduction channel in which shearing and slip can occur on varying planes within this few kilometer wide, heavily deformed subduction channel. The faulting formulation is in that sense comparable to the thick fault zone model presented in similar geodynamic elasto-plastic models [*Lecomte et al*., 2012] and the inelastic-zone or "fault zone" models used to represent faults in dynamic rupture models [e.g., *Dalguer and Day*, 2006]. Despite these limitations, the observations of several dynamic features combined with a reasonable match with the laboratory results and natural observables, give us confidence that our findings can be generalized and used to study seismic cycles at large spatial andtemporal scales.

5. Conclusions

[96] This paper demonstrates that continuum visco-elasto-plastic models, typically used to model large spatial and temporal geodynamic processes, can be used to investigate the long-term seismic cycle, including interseismic strain accumulation, coseismic ruptures, and postseismic creep. Our simulations are validated against a new laboratory approach of a visco-elastic gelatin wedge that is underthrusted by a rigid plate with a velocity-weakening zone surrounded by velocity-strengthening regions (Paper 1). The results for this laboratory setup are valid for both a quasi-static model and the presented model, which includes an incompressible inertia formulation to regularize large slip rates at small time steps.

[97] The effects of the frictional formulation are evaluated through a comparison with analog earthquake source parameters. A purely pressure dependent yield strength, i.e., static friction, produces several velocity reversals indicating elastic events, but lacks consistent strength recovery, a short duration, and rupture speed. A key modification is the incorporation of a velocity-weakening friction within the seismogenic zone to simulate fast and unstable frictional weakening and ensure subsequent healing to build up stresses for the next event. Additionally, velocity-strengthening within the updip and downdip aseismic regions promotes slip complexity and is necessary to decelerate the rupture and thereby match the laboratory results.

[98] In our reference model, slip is a spontaneous outcome of the self-consistent stress and strength build up due to plate convergence, gravity, and the defined frictional properties. Asperities, or areas of increased stress, arise spontaneously both at the edges of the seismogenic zone due to differential coupling and within the seismogenic zone due to the premature arrest of small events. Spontaneous nucleation occurs on one of these heterogeneities, mainly at the largest one at the downdip limit, once a large enough patch yields simultaneously. The resulting rupture propagates as a frictional instability that releases stresses in its wake and increases them just ahead of the rupture front. This instantaneously increases stresses towards their strength, until a too large strength excess arrests the rupture. The majority of ruptures propagate as a crack, although self-healing is observed for several pulses. We also observe re-rupturing of the same fault patch by back-propagation and on one occasion by re-rupturing at the hypocenter.

[99] Finally, the applicability of our approach is demonstrated by surface displacements that are consistent with geodetically observed directions and relative magnitudes. Interseimic displacements move landwards, while uplift starts just seaward of the downdip limit of the seismogenic zone. These displacements are rebound coseismically, and the causative slip at the thrust is best resolved from the vertical component of a station in the center of the seismogenic zone. Postseismic signals include persistent seaward motions on land and high coastal uplift rates due to afterslip and rapid re-locking, respectively.

[100] The ability to reproduce a broad range of observed physical phenomena combined with the accomplished fit to the laboratory results demonstrates that our approach is robust within modeling limitations. This opens a world of interdisciplinary research possibilities, which will likely lead to an increase of our physical understanding of long-term seismic cycles in complex, seismically active subduction zones.

Appendix A: Numerical Stability

[101] The numerical stability of this innovative, continuum visco-elasto-plastic approach is described in the following subsections, where we subsequently discuss the sensitivity and reproducibility of the results (Appendix A1) and the approximate independence of the numerical solution with respect to the temporal (Appendix A2) and spatial resolution (Appendix A3). Potential sources of physical damping that facilitate a stable resolution of frictional instabilities, include viscous dissipation (a physical versions of what is described in e.g., *Shaw and Rice* [2000]), velocity-strengthening friction at larger distances from the source, and inertia to regularize large slip rates at small time steps (Appendix A2). Finally, we comment that implicit time stepping schemes are inherently stable, once convergence is proven, and that the Lagrangian marker-in-cell technique allows for a high degree of stability when advection is involved [*Gerya*, 2010]. The robustness of these schemes is established in previous benchmark for both viscous and elastic [*Gerya*, 2010] and plastic [*Buiter et al*., 2006] rheologies.

A1. Inherent Source Parameter Variation

[102] The seismicity pattern (Figure 4) and source parameter distributions (Figure 5) are fully reproducible and deterministic, in case of identical numerical setup and computational platform. Minor perturbations, such as initial random marker locations, however, can introduce slight changes during one event. This affects the stress distribution for all subsequent events and eliminates the possibility to retrieve the exact same solution. The evaluation of sufficient events, however, always leads to the same statistical results in terms of source parameter distributions. This variability due to the inherent sensitivity of plasticity is demonstrated in Figure A1 for eight experiments run with different, though statistically similar, initial random marker distributions. Single models can show variations of 0–10%, while variations between events within one model can show variations up to hundreds of percents. All these models exhibit the characteristic rupture and surface displacement features observed in this paper.

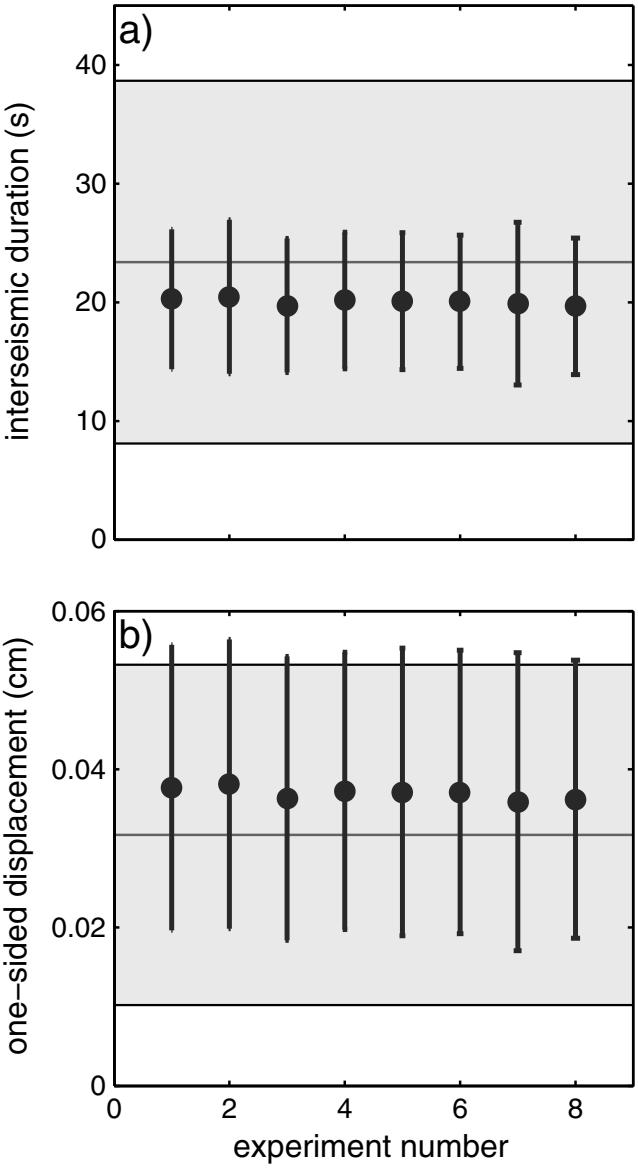

Figure A1. Sensitivity of plasticity as evident from a 0–10% variability in (a) recurrence interval and (b) coseismic one-sided displacement for eight similar numerical simulations with different, though statistically similar, initial random marker distributions. The laboratory average and one standard deviation are shown in grey in the background. The reference experiment analyzed in this paper is experiment number 1.

A2. Time Step and Inertia

[103] The computational time step is used both to solve the conservation equations (Equations (1)–(3)) and to estimate the amount of elastic versus viscous deformation (see section 2.1.2 and Equation (9)). When the time step is varied over a wide range, without including the inertial term, we observe that velocities grow exponentially for decreasing time steps (grey line, Figure A2b). At these velocities, maximum accelerations show that the inertial term is about the same order as the gravity term, and should therefore be included. The acceleration term counteracts the increasing velocities and thereby stabilizes the increasing accelerations and velocities with decreasing time step (black line, Figure A2b). In other words, inertia restrains the runaway behavior when decreasing the time step by balancing the growth of kinetic energy of an accelerating returning wedge with the release of potential energy from accumulated stresses. Other source parameters, like coseismic duration in Figure A2a, are also regularized to reach a small plateau for decreasing time steps. Validity is confirmed by the observation that all source parameters, except the already outlying rupture width, are limited to within one standard deviation of the laboratory parameters for this wide range of analyzed time steps. A similar regularization for exponentially growing velocities during instabilities is applied in rupture models that include radiation damping to stabilize high slip rates by providing an energy outflow in the form of seismic waves [e.g., *Rice*, 1993; *Liu and Rice*, 2005].

[104] A direct comparison of the reference model to an identical model without inertia (black versus grey open

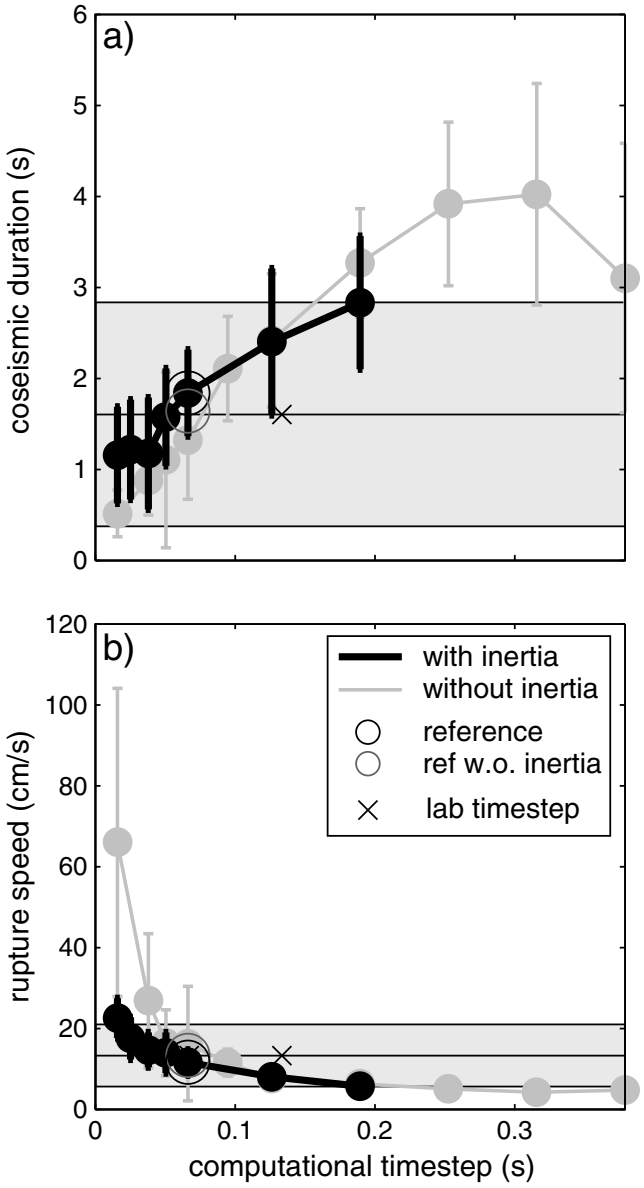

Figure A2. Role of computational or elastic time step illustrated for (a) coseismic duration, and (b) downward rupture speed, combined with the impact of inertia that stabilizes the solution at small time steps (black versus grey lines). Similarly, the black open circle is the reference model, while the grey open circle refers to the same model without inertia. The laboratory one standard deviation range is shown as a grey box and two crosses are added for the frame intervals of the two laboratory cameras. Note that the half width of the event selection algorithm is linearly changed with time step to maintain a constant minimum time between selected peaks.

circle in Figure A2, respectively) shows that the impact of inertia in this laboratory setup is minor. This can be explained by the low characteristic return velocity of the low shear-wave speed gelatin wedge, which has accompanying low accelerations and hence a small inertial term.

[105] Finally, the applied time step (0.066 s) was selected, because it leads to a steady solution for a range of models, including those without inertia and without velocity-strengthening. This gives us confidence the selection was appropriate and it increases the comparison potential for our models. Moreover, it is similar to the 15 fps frame rate used for camera 2 in the laboratory models. Note also that the selected time step is near the maximum time step allowed for the resolution of seismic waves according to the Courant-Friedrichs-Lewy-criterion, as defined for less well constrained Eulerian explicit schemes (0.044 ms).

A3. Grid Size

[106] In typical seismology and geodynamic models, plasticity is grid size dependent and strain rates increase with increasing spatial resolution, if not regularized [e.g., *Vermeer and De Borst*, 1984; *Templeton and Rice*, 2008; *Kaus*, 2010]. Seismic cycle models experiencing this spatial resolution dependency are often described as inherently discrete, which refers to fact that grid cells can fail independently of one another and lead to an incoherent resolution of the problem [e.g., *Rice*, 1993]. By choosing the grid size small enough, the solution of the discrete set of equations can converge toward a continuum limit. In Figure A3 we demonstrate that our solution converges, once a velocity-weakening friction is introduced (compare static friction results in Figure A3a with velocity-weakening friction results in Figure A3b). Static friction models show a variation of recurrence interval of about 40% for a factor 2 change and are hence inherently discrete. Once velocity-weakening friction is introduced, however, the average recurrence interval changes by less than 5% (which is within the models inherent variability). This is achieved by the introduction of a slip velocity formulation in which strain rate is multiplied by grid size (Equation (16)). This multiplication cancels their respective changes and introduces a length scale into the constitutive equations [e.g., *Lavier et al*., 2000]. The implicit regularization of mesh-dependent plasticity through the addition of a rate-dependent material was already demonstrated in computational mechanics [e.g., *Needleman*, 1988].

Appendix B: Scaling

[107] The procedure to scale laboratory values up to natural values is of critical importance when modeling geodynamic processes. This scaling procedure is thoroughly explained in section 2.3 of Paper 1 and the resulting scaling factors, together with the numerical model and natural values, are summarized in Table B1. The key of the procedure is that each important physical dimension, i.e., length, time, and weight, is scaled with a constant factor (i.e., scaling factor) that is derived based on the principals of geometric, kinematic, dynamic, and rheological similarity [e.g., *Hubbert*, 1937; *Ramberg*, 1981; *Weijermars and Schmeling*, 1986]. A scaling factor, denoted by * is a dimensionless number that represents the ratio and the tuning between model (M) and natural (N) quantities. The step-wise procedure to derive these scaling factors from model measurements, is as follows:

[108] First, representative natural values for length L, density ρ, and viscosity η need to be chosen to determine their scaling factors (L^*, ρ^*, η^* resp.). At the same time, the gravity acceleration scaling factor g^* is set to 1, since both the model and the earth's surface processes experience to the same gravity.

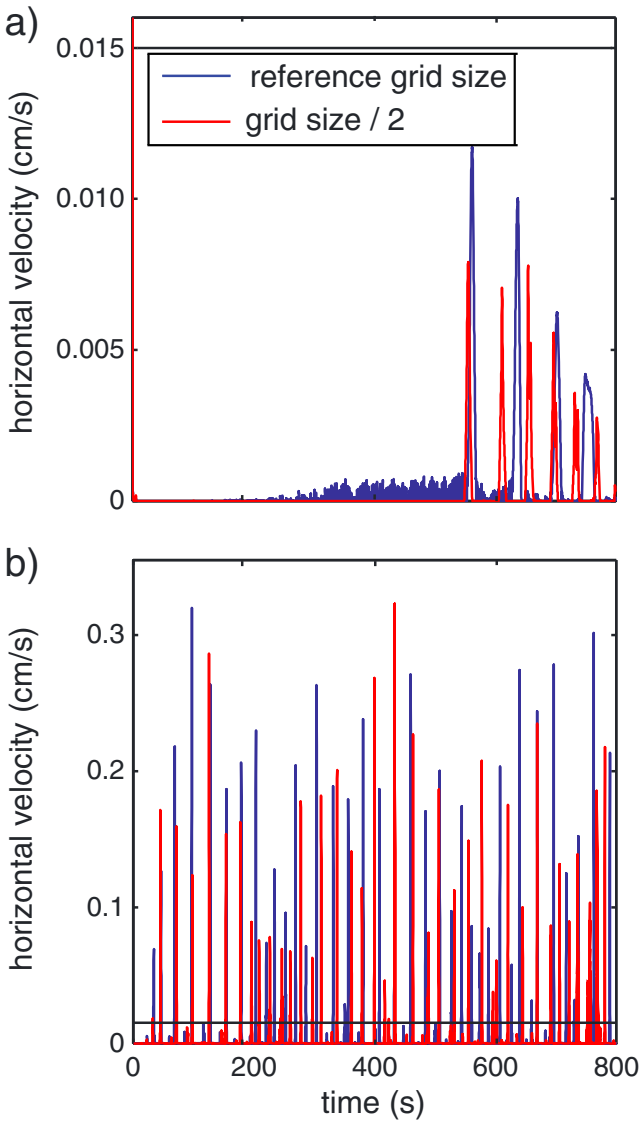

Figure A3. Role of spatial discretization illustrated by plotting maximum horizontal velocities through time for (a) a static friction coefficient, and (b) a purely velocity weakening friction coefficient. Without rate-dependent weakening, the recurrence interval (of slowly returning events) decreases by almost a factor of 2 when halving the grid size, while the same change in a model with rate-dependent weakening experiences a change of less than 5%, which is within the inherent variability of our models (Figure A1). Note that even if we vary grid size over a factor 8, the maximum variation of average recurrence time is only 18%. The horizontal black line indicates the velocity threshold applied.

[109] Second, the stress scaling factor σ^* can be derived from the physical units already selected (Equation (B1)). Shear modulus and cohesion also have stress dimensions, so these need to be scaled with the same factor.

$$\sigma^* = \rho^* \cdot g^* \cdot L^* \tag{B1}$$

[110] The scaling of time T is more complicated due to the different nature and time scales of the seismic cycle processes. This therefore requires two different assumptions valid during the interseismic T_i and coseismic T_c periods [*Rosenau et al.*, 2009].

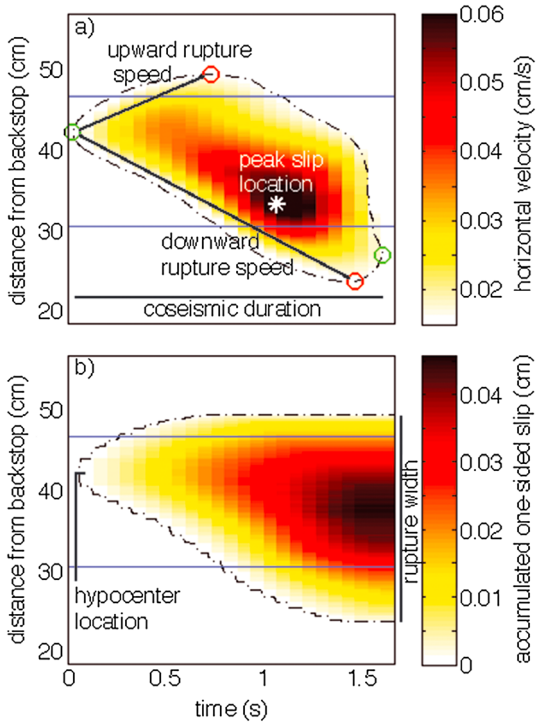

Figure A4. Source parameters derived from (a) spatiotemporal evolution of horizontal velocity for a typical numerical event (at 709 s, also analyzed in Figures 7, 8, and 10). Parameters are derived using the extreme locations (open dots; green for time, and red for space) of the velocity threshold contour (dash-dotted black line). (b) shows the accumulated one-sided slip or rather displacement, which provides an average one-sided displacement once averaged over space. Colored squares are proportional to the spatial and temporal coseismic resolution, demonstrating high resolving power during the coseismic period.

We assume that gravity is the dominant force in the interseismic period, so viscous, slow deformation is important [*Weijermars and Schmeling*, 1986], and

$$T_i^* = \frac{\eta^*}{\sigma^*} \tag{B2}$$

However, during the "instantaneous" coseismic period, we assume inertia should be considered. This requires a constant Froude number $(v \cdot (g \cdot l)^{-0.5})$, i.e., a constant ratio of a body's inertia to gravitational forces, so scaling should follow the dimensions already assumed for gravity acceleration, $L^*/T_c^{*2} = 1$, leading to

$$T_c^* = \sqrt{L^*} \tag{B3}$$

[111] Subsequently, inter- and coseismic velocities scaling factors, v_i^* and v_c^* respectively, can be derived by dividing respective length over time scaling factors.

[112] A discussion about the final natural values in comparison to nature is provided in section 4.3 of Paper 1. In summary, natural upscaled values are within a very broad range of observed values, although slip values are about one order of magnitude too large. Possible reasons include both the absence of two sources that could potentially absorb energy from the rupture, i.e. the absent lateral third dimension [e.g., *Andrews et al.*, 2007] and off-fault

Table B1. Scaling Parameters (*) Converting Simulated Laboratory Values (M) to Natural Equivalents (N) for the Reference Models Input and Resulting Source Parameter Averages

Parameter		P_M / P_N	Model	Nature
Gravity acceleration	g^*	1	$9.81\ m \cdot s^{-2}$	$9.81\ m \cdot s^{-2}$
Depth along backstop	L^*	$1.57 \cdot 10^{-6}$	0.11 m	70 km
Length along surface		$1.57 \cdot 10^{-6}$	0.60 m	381.8 km
One-sided coseismic displacement		$1.57 \cdot 10^{-6}$	$0.37 \cdot 10^{-3}$ m	234.8 m
Rupture width		$1.57 \cdot 10^{-6}$	0.30 m	192.4 km
Recurrence interval	T_i^*	$1.11 \cdot 10^{-10}$	19.3 s	5518 yr
Plate velocity	v_i^*	$1.42 \cdot 10^{4}$	$0.0039\ cm \cdot s^{-1}$	$8.67\ cm \cdot yr^{-1}$
Coseismic duration	T_c^*	$1.25 \cdot 10^{-3}$	1.84 s	24.5 min
Peak one-sided slip velocity	v_c^*	$1.25 \cdot 10^{-3}$	$0.082 \cdot 10^{-2}\ m \cdot s^{-1}$	$0.65\ m \cdot s^{-1}$
Rupture speed average		$1.25 \cdot 10^{-3}$	$0.13\ m \cdot s^{-1}$	$0.11\ km \cdot s^{-1}$
Stress	σ^*	$5.42 \cdot 10^{-7}$	e.g., 60 Pa	110.7 MPa
Cohesion		$5.42 \cdot 10^{-7}$	6 Pa	11.1 MPa
Shear modulus		$5.42 \cdot 10^{-7}$	5000 Pa	9.2 GPa
Viscosity	η^*	$6 \cdot 10^{-17}$	$3 \cdot 10^{5}$ Pa·s	$5 \cdot 10^{21}$ Pa·s
Density	ρ^*	0.345	$1000\ kg \cdot m^{-3}$	$2900\ kg \cdot m^{-3}$

plasticity [e.g., *Dunham et al*., 2011], and a large strength drop due to the significantly more compliant hanging wall [*Ma and Beroza*, 2008]. These too large scaled slip values correspond to the very large scaled recurrence intervals, which could both be explained by a low scaled shear modulus. We also note that our ruptures propagate slowly and are always sub-shear (at about 10% of the shear wave speed).

[113] Finally, we provide a rough estimate of earthquake size, which is potentially overestimated since also slip (and hence rupture width, which is related to it through a power 10) is overestimated in our two-dimensional setting. Using a scaled rupture width, we estimate the missing lateral length of the rupture and corresponding moment magnitude using empirical scaling relations based on subduction interface earthquakes from *Blaser et al*. [2010]. This empirical scaling procedure leads to moment magnitudes ranging from 7.2 up to 9.3 for our simulated events.

Appendix C: Source Parameter Derivation

[114] A more detailed, quantitative analysis of the spatio-temporal horizontal velocity pattern (as explained in section 3.1.1 and more in detail in section 2.6 of the companion paper) is done by analyzing each event in Figure 4c separately. The extremes of the contour defined by the velocity threshold are used to select; a) hypocenter depth, b) rupture width (defined by extremes in space), c) coseismic duration (defined by extremes in time), and d) the average upward and downward rupture speeds (defined by a division of upward or downward spatial extent with respect to the hypocenter over duration until those points). The recurrence interval is defined by the time between the end of the preceding and the start of the next event. The spatial distribution of coseismic single-sided displacement is calculated by cumulating coseismic displacements (Figure A4b). The spatial average of this leads to the average one-sided, coseismic displacement, which is equal to the slip if subducting plate displacements would be added.

[115] **Acknowledgments.** We thank two anonymous reviewers and the Associate Editor, Jean Paul Ampuero, for their constructive reviews. This research benefited from stimulating discussions with Alice Gabriel, Ralph Archuleta, and Raul Madariaga on rupture dynamics and geodetic displacements, with Arnauld Heuret on observational insights from subduction zone earthquakes, with Giorgio Ranalli on scaling, and with Domenico Giardini and Gabriele Morra, who are also thanked for supporting this exciting multi-disciplinary project. This research was supported by SNSF grant 200021-125274 and the EURYI (European Young Investigators) Awards Scheme (Eurohorcs/ESF, responsible F.F.).

References

Abe, K. (1975), Static and dynamic fault parameters of the Saitama earthquake of July 1, 1968, *Tectonophysics*, *27*(3), 223–238.

Ampuero, J.-P., and Y. Ben Zion (2008), Cracks, pulses and macroscopic asymmetry of dynamic rupture on a bimaterial interface with velocity-weakening friction, *Geophys. J. Int.*, *173*, 674–692.

Andrews, D. J., T. C. Hanks, and J. W. Whitney (2007), Physical Limits on Ground Motion at Yucca Mountain, *Bull. Seismol. Soc. Am.*, *97*(6), 1771–1792.

Aoki, Y., and C. H. Scholz (2003), Vertical deformation of the Japanese islands, 1996–1999, *J. Geophys. Res.*, *108*(B5), 2257, doi:10.1029/2002JB002129.

Barrientos, S. E., G. Plafker, and E. Lorca (1992), Postseismic coastal uplift in southern Chile, *Geophys. Res. Lett.*, *19*(7), 701.

Ben-Zion, Y. (2008), Collective behavior of earthquakes and faults: Continuum-discrete transitions, progressive evolutionary changes, and different dynamic regimes, *Rev. Geophys.*, *46*(4).

Ben-Zion, Y., and J. R. Rice (1995), Slip patterns and earthquake populations along different classes of faults in elastic solids, *J. Geophys. Res.*, *100*(12), 12.

Ben-Zion, Y., and J. R. Rice (1997), Dynamic simulations of slip on a smooth fault in an elastic solid, *J. Geophys. Res.*, *102*, 17,771–17,784.

Beroza, G. C., and T. Mikumo (1996), Short slip duration in dynamic rupture in the presence of heterogeneous fault properties, *J. Geophys. Res.*, *101*, 22–22.

Bilek, S., and T. Lay (2002), Tsunami earthquakes possibly widespread manifestations of frictional conditional stability, *Geophys. Res. Lett.*, *29*(14), 18–11.

Blaser, L., F. Kruger, M. Ohrnberger, and F. Scherbaum (2010), Scaling Relations of Earthquake Source Parameter Estimates with Special Focus on Subduction Environment, *Bull. Seismol. Soc. Am.*, *100*(6), 2914–2926.

Brackbill, J., and H. Ruppel (1986), FLIP: A method for adaptively zoned, particle-in-cell calculations of fluid flows in two dimensions, *J. Comput. Phys.*, *65*(2), 314–343.

Buiter, S., A. Babeyko, S. Ellis, T. Gerya, B. Kaus, A. Kellner, G. Schreurs, and Y. Yamada (2006), The numerical sandbox: comparison of model results for a shortening and an extension experiment, *Analogue and Numerical Modelling of Crustal-Scale Processes*, *253*, 29–64.

Burridge, R., and L. Knopoff (1967), Model and theoretical seismicity, *Bull. Seismol. Soc. Am.*, *57*(3), 341–371.

Byrne, D. E., D. M. Davis, and L. R. Sykes (1988), Loci and maximum size of thrust earthquakes and the mechanics of the shallow region of subduction zones, *Tectonics*, *7*(4), 833–857.

Carlson, J., and J. Langer (1989), Mechanical model of an earthquake fault, *Phys. Rev. A*, *40*(11), 6470–6484.

Cattin, R., and J. Avouac (2000), Modeling mountain building and the seismic cycle in the Himalaya of Nepal, *J. Geophys. Res.*, *105*(B6), 13,389–13,407.

Chery, J., and P. Vernant (2006), Lithospheric elasticity promotes episodic fault activity, *Earth Planet Sci. Lett.*, *243*(1-2), 211–217.

Cochard, A., and R. Madariaga (1994), Dynamic faulting under rate-dependent friction, *Pure Appl. Geophys.*, *142*(3/4), 419–445.

Cochard, A., and R. Madariaga (1996), Complexity of seismicity due to highly rate-dependent friction, *J. Geophys. Res.*, *101*(B11), 25,321–25,336.

Cohen, S. (1994), Evaluation of the Importance of Model Features For Cyclic4Deformation Due to Dipâ€Slip Faulting, *Geophys. J. Int.*, *119*(3), 831–841.

Corbi, F., F. Funiciello, C. Faccenna, G. Ranalli, and A. Heuret (2011), Seismic variability of subduction thrust faults: Insights from laboratory models, *J. Geophys. Res.*, *116*(B6), B06304.

Corbi, F., F. Funiciello, M. Moroni, Y. van Dinther, P. M. Mai, L. A. Dalguer, and C. Faccenna (2013), The seismic cycle at subduction thrusts: 1. insights from laboratory models, *J. Geophys. Res.*, doi:10.1029/2012JB009481, in press.

Crameri, F., et al. (2011), A benchmark comparison of numerical topography - what are suitable sticky air parameters?, *Geophys. J. Int.*, *200*, 1–12.

Dalguer, L., and S. Day (2006), Comparison of fault representation methods in finite difference simulations of dynamic rupture, *Bull. Seismol. Soc. Am.*, *96*(5), 1764.

Das, S., and C. H. Scholz (1983), Why large earthquakes do not nucleate at shallow depths, *Nature*, *305*(5935), 621–623.

Daub, E., and J. Carlson (2008), A constitutive model for fault gouge deformation in dynamic rupture simulations, *J. Geophys. Res.*, *113*, B12309.

Daub, E. G., and J. M. Carlson (2009), Stick-slip instabilities and shear strain localization in amorphous materials, *Phys. Rev. E*, *80*(6).

Daub, E. G., M. L. Manning, and J. M. Carlson (2010), Pulse-like, crack-like, and supershear earthquake ruptures with shear strain localization, *J. Geophys. Res.*, *115*(B5).

de la Puente, J., J.-P. Ampuero, and M. Kaser (2009), Dynamic rupture modeling on unstructured meshes using a discontinuous Galerkin method, *J. Geophys. Res.*, *114*(B10).

Di Giuseppe, E., F. Funiciello, F. Corbi, G. Ranalli, and G. Mojoli (2009), Gelatins as rock analogs: A systematic study of their rheological and physical properties, *Tectonophysics*, *473*(3-4), 391–403.

Di Toro, G., R. Han, T. Hirose, N. D. Paola, S. Nielsen, K. Mizoguchi, F. Ferri, M. Cocco, and T. Shimamoto (2011), Fault lubrication during earthquakes, *Nature*, *471*(7339), 494–499.

Dieterich, J. (1979), Modeling of Rock Friction 1. Experimental Results and Constitutive Equation, *J. Geophys. RGeological Society of America Bulletines.*, *84*, 2161–2168.

Dieterich, J. (2007), Applications of Rate- and State-Dependent Friction to Models of Fault Slip and Earthquake Occurrence, Treatise of Geophysics, pp. 107–126.

Dieterich, J., and K. Richards-Dinger (2010), Earthquake recurrence in simulated fault systems, *Pure Appl. Geophys.*, *167*(2010), 1087–1104.

Dixon, T. H. (1993), GPS measurement of relative motion of the Cocos and Caribbean Plates and strain accumulation across the Middle America Trench, *Geophys. Res. Lett.*, *20*(20), 2167–2170.

Dmowska, R., J. Rice, L. Lovison, and D. Josell (1988), Stress transfer and seismic phenomena in coupled subduction zones during the earthquake cycle, *J. Geophys. Res.*, *93*, 7869–7884.

Dmowska, R., G. Zheng, and J. Rice (1996), Seismicity and deformation at convergent margins due to heterogeneous coupling, *J. Geophys. Res.*, *101*, 3015–3029.

Drucker, D., and W. Prager (1952), Soil mechanics and plastic analysis for limit design, *Q. Appl. Math*, *10*, 157–165.

Duan, B., and D. Oglesby (2005), The dynamics of thrust and normal faults over multiple earthquake cycles: effects of dipping fault geometry, *Bull. Seismol. Soc. Am.*, *95*(5), 1623–1636.

Dunham, E. M., D. Belanger, L. Cong, and J. E. Kozdon (2011), Earthquake Ruptures with Strongly Rate-Weakening Friction and Off-Fault Plasticity, Part 1: Planar Faults, *Bull. Seismol. Soc. Am.*, *101*(5), 2296–2307.

Falk, M., and J. Langer (1998), Dynamics of viscoplastic deformation in amorphous solids, *Phys. Rev. E*, *57*(6), 7192.

Fuji, Y., and N. Katsumi (1983), Horizontal crustal movements in the Kanto-Tokai district, Japan, as decuded from geodetic data, *Tectonophysics*, *97*, 115–140.

Fuller, C., S. Willett, and M. Brandon (2006), Formation of forearc basins and their influence on subduction zone earthquakes, *Geology*, *34*(2), 65–68.

Gabriel, A. A., J.-P. Ampuero, L. A. Dalguer, and P. M. Mai (2012), The transition of dynamic rupture styles in elastic media under velocity-weakening friction, *J. Geophys. Res.*, *117*(B9), B09311.

Gerya, T. (2010), Introduction to numerical geodynamic modelling, Cambridge University Press, Cambridge, U.K.

Gerya, T. (2011), Future directions in subduction modeling, *J. Geodyn.*, *52*, 344–378.

Gerya, T., and D. Yuen (2007), Robust characteristics method for modelling multiphase visco-elasto-plastic thermo-mechanical problems, *Phys. Earth Planet In.*, *163*(1-4), 83–105.

Gerya, T. V., and D. Yuen (2003), Characteristics-based marker-in-cell method with conservative finite-differences schemes for modeling geological flows with strongly variable transport properties, *Phys. Earth Planet In.*, *140*(4), 293–318.

Gorczyk, W., A. Willner, T. Gerya, J. Connolly, and J. Burg (2007), Physical controls of magmatic productivity at Pacific-type convergent margins: Numerical modelling, *Phys. Earth Planet. In.*, *163*(1-4), 209–232.

Hashimoto, C., and M. Matsu'ura (2002), 3-D Simulation of Earthquake Generation Cycles and Evolution of Fault Constitutitve Properties, *Pure Appl. Geophys.*, *159*(10), 2175–2199.

Heaton, T. (1990), Evidence for and implications of self-healing pulses of slip in earthquake rupture, *Phys. Earth Planet. In.*, *64*(1), 1–20.

Heuret, A., S. Lallemand, F. Funiciello, C. Piromallo, and C. Faccenna (2011), Physical characteristics of subduction interface type seismogenic zones revisited, *Geochem. Geophys. Geosyst.*, *12*(1), Q01004.

Hill, R. (1950), The Mathematical Theory of Plasticity, Oxford University Press, Oxford.

Hillers, G., Y. Ben-Zion, and P. Mai (2006), Seismicity on a fault controlled by rate-and state-dependent friction with spatial variations of the critical slip distance, *J. Geophys. Res.*, *111*(B01403), 23.

Hillers, G., P. M. Mai, Y. Ben-Zion, and J.-P. Ampuero (2007), Statistical properties of seismicity of fault zones at different evolutionary stages, *Geophys. J. Int.*, *169*(2), 515–533.

Hirahara, K. (2002), Interplate earthquake fault slip during periodic earthquake cycles in a viscoelastic medium at a subduction zone, *Pure Appl. Geophys.*, *159*(10), 2201–2220.

Hori, T., and S. Miyazaki (2011), A possible mechanism of M9 earthquake generation cycles in the area of repeating M78 earthquakes surrounded by aseismic sliding, *Earth Planets Space*, *63*(7), 773–777.

Hsu, Y. J., M. Simons, J.-P. Avouac, J. Galetzka, K. Sieh, M. Chlieh, D. Natawidjaja, L. Prawirodirdjo, and Y. Bock (2006), Frictional Afterslip Following the 2005 Nias-Simeulue Earthquake, Sumatra, *Science*, *312*(5782), 1921–1926.

Hubbert, M. (1937), Theory of scale models as applied to the study of geologic structures, *Bull. Geol. Soc. Am.*, *48*(10), 1459–1519.

Huc, M., R. Hassani, and J. Chery (1998), Large earthquake nucleation associated with stress exchange between middle and upper crust, *Geophys. Res. Lett.*, *25*(4), 551–554.

Hudnut, K. (2011), The 4 April 2010 El Mayor-Cucapah earthquake source, from initial glimpse to synoptic overview, presented at 2011 Annual Meeting, SCEC, Palm Springs, California, available online at http://www.scec.org/meetings/2011am/emc.html.

Ide, S., A. Baltay, and G. C. Beroza (2011), Shallow Dynamic Overshoot and Energetic Deep Rupture in the 2011 Mw 9.0 Tohoku-Oki Earthquake, *Science*, *332*(6036), 1426–1429.

Ito, T., K. Ozawa, T. Watanabe, and T. Sagiya (2011), Slip distribution of the 2011 off the Pacific coast of Tohoku Earthquake inferred from geodetic data, *Earth Planets Space*, *63*(7), 627–630.

Kaneko, Y., and N. Lapusta (2008), Variability of earthquake nucleation in continuum models of rate-and-state faults and implications for aftershock rates, *J. Geophys. Res.*, *113*, B12312, doi:10.1029/2007JB005154.

Kaneko, Y., N. Lapusta, and J. Ampuero (2008), Spectral element modeling of spontaneous earthquake rupture on rate and state faults: Effect of velocity-strengthening friction at shallow depths, *J. Geophys. Res.*, *113*(B9), B09317.

Kaneko, Y., J. Avouac, and N. Lapusta (2010), Towards inferring earthquake patterns from geodetic observations of interseismic coupling, *Nat. Geosci.*, *3*, 363–369, doi:10.1038/NGEO843.

Kato, N., and T. Hirasawa (1997), A numerical study on seismic coupling along subduction zones using a laboratory-derived friction law, *Phys. Earth Planet In.*, *102*(1–2), 51–68.

Kaus, B. (2010), Factors that control the angle of shear bands in geodynamic numerical models of brittle deformation, *Tectonophysics*, *484*, 36–47.

Khazaradze, G., and J. Klotz (2003), Short- and long-term effects of GPS measured crustal deformation rates along the south central Andes, *J. Geophys. Res.*, *108*(B6).

Lapusta, N., and J. R. Rice (2003), Nucleation and early seismic propagation of small and large events in a crustal earthquake model, *J. Geophys. Res.*, *108*(B4), 2205.

Lapusta, N., J. Rice, Y. Ben-Zion, and G. Zheng (2000), Elastodynamic analysis for slow tectonic loading with spontaneous rupture episodes on faults with rate- and state-dependent friction, *J. Geophys. Res.*, *105*(B10), 23,765–23,789.

Lavier, L. L., W. R. Buck, and A. N. B. Poliakov (2000), Factors controlling normal fault offset in an ideal brittle layer, *J. Geophys. Res.*, *105*(23), 431–423.

Lecomte, E., L. Le Pourhiet, O. Lacombe, and L. Jolivet (2011), A continuum mechanics approach to quantify brittle strain on weak faults: application to the extensional reactivation of shallow dipping discontinuities, *Geophys. J. Int.*, *184*(1), 1–11.

Lecomte, E., L. Le Pourhiet, and O. Lacombe (2012), Mechanical basis for slip along low-angle normal faults, *Geophys. Res. Lett.*, *39*(3).

Liu, Y., and J. R. Rice (2005), Aseismic slip transients emerge spontaneously in three-dimensional rate and state modeling of subduction earthquake sequences, *J. Geophys. Res.*, *110*(B08307), 1–14.

Lu, X., N. Lapusta, and A. J. Rosakis (2010), Pulse-like and crack-like dynamic shear ruptures on frictional interfaces: experimental evidence, numerical modeling, and implications, *Int J Fract.*, *163*(1–2), 27–39.

Lyakhovsky, V., and Y. Ben-Zion (2008), Scaling relations of earthquakes and aseismic deformation in a damage rheology model, *Geophys. J. Int.*, *172*(2), 651–662.

Lyakhovsky, V., and Y. Ben-Zion (2009), Evolving geometrical and material properties of fault zones in a damage rheology model, *Geochem. Geophys. Geosyst.*, *10*(11), Q11011.

Lyakhovsky, V., Y. Ben-Zion, and A. Agnon (2001), Earthquake cycle, fault zones, and seismicity patterns in a rheologically layered lithosphere, *J. Geophys. Res.*, *106*, 4103–4120.

Lyakhovsky, V., Y. Hamiel, and Y. Ben-Zion (2011), A non-local visco-elastic damage model and dynamic fracturing, *J Mech Phys Solid*, *59*, 1752–1776.

Ma, S., and G. C. Beroza (2008), Rupture Dynamics on a Bimaterial Interface for Dipping Faults, *Bull. Seismol. Soc. Am.*, *98*(4), 1642–1658.

Madariaga, R., and K. Olsen (2002), Earthquake dynamics, in International Handbook of Earthquake and Engneering Seismology, pp. 175–194, Academic Press, London, U.K.

Marone, C., and C. H. Scholz (1988), The depth of seismic faulting and the upper transition from stable to unstable slip regimes, *Geophys. Res. Lett.*, *15*(6), 621–624.

Meng, L., J.-P. Ampuero, M. T. Page, and K. W. Hudnut (2011), Seismological evidence and dynamic model of reverse rupture propagation during the 2010 M7.2 El Mayor - Cucapah earthquake, Abstract S52B-04 presented at 2011 Fall Meeting, AGU, San Francisco, California, 5-9 Dec.

Moreno, M., M. Rosenau, and O. Oncken (2010), 2010 Maule earthquake slip correlates with pre-seismic locking of Andean subduction zone, *Nature*, *467*, 198–202.

Moresi, L., F. Dufour, and H. Mühlhaus (2003), A Lagrangian integration point finite element method for large deformation modeling of viscoelastic geomaterials, *J. Comput. Phys.*, *184*(2), 476–497.

Needleman, A. (1988), Material rate dependence and mesh sensitivity in localization problems, *Comput. Meth. Appl. Mech. Eng.*, *67*(1), 69–85.

Nielsen, S., J. Taddeucci, and S. Vinciguerra (2010), Experimental observation of stick-slip instability fronts, *Geophys. J. Int.*, *180*(2), 697–702.

Noda, H., and N. Lapusta (2010), Three-dimensional earthquake sequence simulations with evolving temperature and pore pressure due to shear heating: Effect of heterogeneous hydraulic diffusivity, *J. Geophys. Res.*, *115*(B12).

Ohnaka, M. (2004), Earthquake cycles and physical modeling of the process leading up to a large earthquake, *Earth Planets Space*, *56*(8), 773–794.

Olsen, K., et al. (2009), ShakeOut-D: Ground motion estimates using an ensemble of large earthquakes on the southern San Andreas fault with spontaneous rupture propagation, *Geophys. Res. Lett.*, *36*(4).

Perfettini, H., and J.-P. Avouac (2004), Postseismic relaxation driven by brittle creep: A possible mechanism to reconcile geodetic measurements and the decay rate of aftershocks, application to the Chi-Chi earthquake, Taiwan, *J. Geophys. Res.*, *109*(B2), B02304.

Perfettini, H., J. P. Avouac, and J. C. Ruegg (2005), Geodetic displacements and aftershocks following the 2001 Mw = 8.4 Peru earthquake: Implications for the mechanics of the earthquake cycle along subduction zones, *J. Geophys. Res.*, *110*(B9), B09404.

Plafker, G. (1972), Alaskan Earthquake of 1964 and Chilean Earthquake of 1960: Implications for Arc Tectonics, *J. Geophys. Res.*, *77*(5), 901–925.

Ramberg, H. (1981), Gravity, deformation, and the earth's crust: In theory, experiments, and geological application, Academic Press London, London, U.K.

Ranalli, G. (1995), *Rheology of the Earth*, 2 ed., Chapman and Hall, London.

Reid, H. (1910), On mass-movements in tectonic earthquakes, *Tech. rep.*, Washington, D.C.

Rice, J. (1993), Spatio-temporal complexity of slip on a fault, *J. Geophys. Res.*, *98*, 9885–9907.

Rosakis, A., K. Xia, G. Lykotrafitis, and H. Kanamori (2007), Dynamic Shear Rupture in Frictional Interfaces: Speeds, Directionality and Modes, in *Treatise in geophysics*, edited by G. Schubert and H. Kanamori, pp. 153–192, Elsevier, Amsterdam.

Rosenau, M., J. Lohrmann, and O. Oncken (2009), Shocks in a box: An analogue model of subduction earthquake cycles with application to seismotectonic forearc evolution, *J. Geophys. Res.*, *114*(B1), B01409.

Rubinstein, J. L., W. L. Ellsworth, N. M. Beeler, B. D. Kilgore, D. A. Lockner, and H. M. Savage (2012), Fixed recurrence and slip models better predict earthquake behavior than the time- and slip-predictable models: 2. Laboratory earthquakes, *J. Geophys. Res.*, *117*, B02307, doi:10.1029/2011JB008723.

Ruina, A. (1983), Slip instability and state variable friction laws, *J. Geophys. Res.*, *88*(10), 359–310.

Saffer, D. M., and C. Marone (2003), Comparison of smectite- and illite-rich gouge frictional properties: application to the updip limit of the seismogenic zone along subduction megathrusts, *Earth Planet Sci. Lett.*, *215*(1–2), 219–235.

Savage, J. (1983), A dislocation model of strain accumulation and release at a subduction zone, *J. Geophys. Res.*, *88*(6), 4984–4996.

Savage, J., and R. Burford (1970), Accumulation of tectonic strain in California, *Bull. Seismol. Soc. Am.*, *60*(6), 1877–1896.

Savage, J., J. Svarc, and W. Prescott (1999), Deformation across the Alaska-Aleutian subduction zone near Kodiak, *Geophys. Res. Lett.*, *26*(14), 2117–2120.

Schmalholz, S., Y. Podladchikov, and D. Schmid (2001), A spectral/finite difference method for simulating large deformations of heterogeneous, viscoelastic materials, *Geophys. J. Int.*, *145*(1), 199–208.

Scholz, C. (1998), Earthquakes and friction laws, *Nature*, *391*(6662), 37–42.

Shaw, B. E., and J. R. Rice (2000), Existence of continuum complexity in the elastodynamics of repeated fault ruptures, *J. Geophys. Res.*, *105*(B10), 23,791–23,810.

Simons, M., et al. (2011), The 2011 magnitude 9.0 Tohoku-Oki earthquake: Mosaicking the megathrust from seconds to centuries, *Science*, *332*, 1421–1425.

Sleep, N. (2002), Self-organization of crustal faulting and tectonics, *Int. Geol. Rev.*, *44*(1), 83–96.

Stuart, W. (1988), Forecast model for great earthquakes at the Nankai trough subduction zone, *Pure Appl. Geophys.*, *126*(2), 619–641.

Templeton, E. L., and J. R. Rice (2008), Off-fault plasticity and earthquake rupture dynamics: 1. Dry materials or neglect of fluid pressure changes, *J. Geophys. Res.*, *113*(B9), B09306.

Thatcher, W. (1983), Nonlinear Strain Buildup and the Earthquake Cycle, *J. Geophys. Res.*, *88*(B7), 5893–5902.

Thatcher, W. (1984), The Earthquake Deformation Cycle at the Nankai Trough, Southwest Japan, *J. Geophys. Res.*, *89*(B5), 3087–3101.

Tse, S., and J. R. Rice (1986), Crustal earthquake instability in relation to the depth variation of frictional slip properties, *J. Geophys. Res.*, *91*(B9), 9452–9472.

Vermeer, P. A. (1990), The orientation of shear bands in biaxial tests, *Géotechnique*, *40*(2), 223–236.

Vermeer, P. A., and R. De Borst (1984), Non-associated plasticity for soilds, concrete, and rock, *Heron*, *29*(3), 1–65.

Wang, J. (1996), Velocity-weakening friction as a factor in controlling the frequency-magnitude relation of earthquakes, *Bull. Seismol. Soc. Am.*, *86*(3), 701–713.

Wang, K. (2007), Elastic and Viscoelastic Models of Crustal Deformation in Subduction Earthquake Cycles, in *The Seismogenic Zone of Subduction Thrust Faults*, edited by T. Dixon and J. Moore, pp. 540–575, Columbia University Press, New York.

Wang, K., and J. He (2008), Effects of frictional behavior and geometry of subduction fault on coseismic seafloor deformation, *Bull. Seismol. Soc. Am.*, *98*(2), 571–579.

Wang, K., and Y. Hu (2006), Accretionary prisms in subduction earthquake cycles: The theory of dynamic Coulomb wedge, *J. Geophys. Res.*, *111*, B06410, 16.

Wang, K., Y. Hu, and J. He (2012), Deformation cycles of subduction earthquakes in a viscoelastic Earth, *Nature*, *484*(7394), 327–332.

Weijermars, R., and H. Schmeling (1986), Scaling of Newtonian and non-Newtonian fluid dynamics without inertia for quantitative modelling of rock flow due to gravity (including the concept of rheological similarity), *Phys Earth Planet In.*, *43*(4), 316–330.

Zaleski, S., and P. Julien (1992), Numerical simulation of Rayleigh-Taylor instability for single and multiple salt diapirs, *Tectonophysics*, *206*(1–2), 55–69.

Zhao, S., and S. Takemoto (2000), Deformation and stress change associated with plate interaction at subduction zones: a kinematic modelling, *Geophys. J. Int.*, *142*(2), 300–318.

Zheng, G., and J. R. Rice (1998), Conditions under which velocity-weakening friction allows a self-healing versus a cracklike mode of rupture, *Bull. Seismol. Soc. Am.*, *88*(6), 1466–1483.

Zöller, G., S. Hainzl, Y. Ben-Zion, and M. Holschneider (2006), Earthquake activity related to seismic cycles in a model for a heterogeneous strike-slip fault, *Tectonophysics*, *423*(1–4), 137–145.